



# Rapid image deconvolution and multiview fusion for optical microscopy

Min Guo<sup>1,22</sup>, Yue Li<sup>1,22</sup>, Yijun Su<sup>1</sup>, Talley Lambert<sup>3,4</sup>, Damian Dalle Nogare<sup>5</sup>, Mark W. Moyle<sup>6</sup>, Leighton H. Duncan<sup>6</sup>, Richard Ikegami<sup>6</sup>, Anthony Santella<sup>7</sup>, Ivan Rey-Suarez<sup>1,8</sup>, Daniel Green<sup>9</sup>, Anastasia Beiriger<sup>10</sup>, Jiji Chen<sup>11</sup>, Harshad Vishwasrao<sup>11</sup>, Sundar Ganesan<sup>12</sup>, Victoria Prince<sup>10,13</sup>, Jennifer C. Waters<sup>3</sup>, Christina M. Annunziata<sup>9</sup>, Markus Hafner<sup>14</sup>, William A. Mohler<sup>15</sup>, Ajay B. Chitnis<sup>5</sup>, Arpita Upadhyaya<sup>8,16,17</sup>, Ted B. Usdin<sup>18</sup>, Zhirong Bao<sup>7</sup>, Daniel Colón-Ramos<sup>6,19,20</sup>, Patrick La Riviere<sup>19,21</sup>, Huafeng Liu<sup>2,22</sup>, Yicong Wu<sup>1,22</sup> and Hari Shroff<sup>1,11,19</sup>

The contrast and resolution of images obtained with optical microscopes can be improved by deconvolution and computational fusion of multiple views of the same sample, but these methods are computationally expensive for large datasets. Here we describe theoretical and practical advances in algorithm and software design that result in image processing times that are ten-fold to several thousand fold faster than with previous methods. First, we show that an ‘unmatched back projector’ accelerates deconvolution relative to the classic Richardson-Lucy algorithm by at least tenfold. Second, three-dimensional image-based registration with a graphics processing unit enhances processing speed 10- to 100-fold over CPU processing. Third, deep learning can provide further acceleration, particularly for deconvolution with spatially varying point spread functions. We illustrate our methods from the subcellular to millimeter spatial scale on diverse samples, including single cells, embryos and cleared tissue. Finally, we show performance enhancement on recently developed microscopes that have improved spatial resolution, including dual-view cleared-tissue light-sheet microscopes and reflective lattice light-sheet microscopes.

Fluorescence microscopy enables imaging with submicrometer spatial resolution, molecular specificity and high contrast. These attributes allow direct interrogation of biological structure and function, yet intrinsic blurring and noise degrade fluorescence data, yielding an imperfect estimate of the underlying sample. Provided the imaging process can be characterized, such degradation can be partially reversed using deconvolution<sup>1,2</sup>, resulting in improved resolution and contrast. For example, given the point spread function (PSF) and data corrupted by Poisson noise (often dominant in fluorescence microscopy), the Richardson–Lucy deconvolution (RLD)<sup>3,4</sup> procedure deblurs the estimate of sample density with each iteration. In addition to deblurring, deconvolution can be used to combine multiple independent measurements taken on the same sample to produce an improved overall estimate of the sample<sup>5</sup>. This approach is especially useful in reconstructing

super-resolution images in structured illumination microscopy<sup>6,7</sup> or in performing joint deconvolution to improve spatial resolution in multiview light-sheet microscopy<sup>8–12</sup>.

Iterative deconvolution has been useful in these applications, but obtaining a resolution-limited result with RLD usually requires ten or more iterations. While the associated computational burden is manageable for single-view microscopes, deconvolving large multiview datasets can take days<sup>12,13</sup>, in many cases drastically exceeding the time for data acquisition.

Here we develop tools that address this problem. First, we show that in most cases the number of iterations can be reduced to one when using an unmatched back projector, fundamentally speeding iterative deconvolution. Second, we optimize three-dimensional (3D) image-based registration methods for efficient multiview fusion and deconvolution on graphics processing unit (GPU) cards.

<sup>1</sup>Laboratory of High-Resolution Optical Imaging, National Institute of Biomedical Imaging and Bioengineering, National Institutes of Health, Bethesda, MD, USA. <sup>2</sup>State Key Laboratory of Modern Optical Instrumentation, College of Optical Science and Engineering, Zhejiang University, Hangzhou, China.

<sup>3</sup>Department of Cell Biology, Harvard Medical School, Boston, MA, USA. <sup>4</sup>Department of Systems Biology, Harvard Medical School, Boston, MA, USA.

<sup>5</sup>Section on Neural Developmental Dynamics, Division of Developmental Biology, Eunice Kennedy Shriver National Institute of Child Health and Human Development, National Institutes of Health, Bethesda, MD, USA. <sup>6</sup>Departments of Neuroscience and Cell Biology, Yale University School of Medicine, New Haven, CT, USA. <sup>7</sup>Developmental Biology Program, Sloan Kettering Institute, New York, NY, USA. <sup>8</sup>Biophysics Program, University of Maryland, College Park, MD, USA. <sup>9</sup>Women’s Malignancies Branch, Center for Cancer Research, National Cancer Institute, Bethesda, MD, USA. <sup>10</sup>Committee on

Development, Regeneration and Stem Cell Biology, University of Chicago, Chicago, IL, USA. <sup>11</sup>Advanced Imaging and Microscopy Resource, National Institutes of Health, Bethesda, MD, USA. <sup>12</sup>Biological Imaging Section, Research Technologies Branch, National Institute of Allergy and Infectious Diseases, National Institutes of Health, Bethesda, MD, USA. <sup>13</sup>Department of Organismal Biology and Anatomy, University of Chicago, Chicago, IL, USA. <sup>14</sup>Laboratory of Muscle Stem Cells and Gene Regulation, National Institute of Arthritis and Musculoskeletal and Skin Diseases, Bethesda, MD, USA. <sup>15</sup>Department of

Genetics and Genome Sciences and Center for Cell Analysis and Modeling, University of Connecticut Health Center, Farmington, CT, USA. <sup>16</sup>Department of Physics, University of Maryland, College Park, MD, USA. <sup>17</sup>Institute for Physical Science and Technology, University of Maryland, College Park, MD, USA. <sup>18</sup>Section on Fundamental Neuroscience, National Institute of Mental Health, National Institutes of Health, Bethesda, MD, USA. <sup>19</sup>Marine Biological Laboratory Fellows Program, Woods Hole, MA, USA. <sup>20</sup>Instituto de Neurobiología, Recinto de Ciencias Médicas, Universidad de Puerto Rico, San Juan, Puerto Rico. <sup>21</sup>Department of Radiology, University of Chicago, Chicago, IL, USA. <sup>22</sup>These authors contributed equally: Min Guo, Yue Li.

<sup>22</sup>e-mail: liuhf@zju.edu.cn; yicong.wu@nih.gov

Finally, we show that computationally intensive deconvolution with a spatially varying PSF can be accelerated by using convolutional neural networks to ‘learn’ the relevant operations, provided that suitable training data can be assembled. These advances result in a speed-up factor of ten- to several thousand-fold over previous efforts. We illustrate the advantages on subcellular to macroscopic length scales, using samples that include single cells, zebrafish and nematode embryos and mouse tissue. In addition to demonstrating improvements on super-resolution and large multiview datasets acquired with state-of-the-art microscopes, we also show that our methods enable the use of new microscopes, including dual-view cleared-tissue light-sheet microscopy and reflective lattice light-sheet (LLS) microscopy.

## Results

**Drastically reducing the number of iterations in iterative deconvolution.** Iterative deconvolution algorithms attempt to estimate the underlying sample density from noisy, blurred images. Important components of such algorithms are a ‘forward projector’, which describes the mapping from the desired image of the object to the noisy, blurred image measured by the microscope, and a ‘back projector’, which maps the measured image back onto the desired object image. For example, in RLD:

$$e_{k+1} = e_k \left\{ \left[ \frac{i}{e_k^* f} \right]^* b \right\}$$

where  $e_k$  is the  $k$ th (current) estimate of the desired object image  $o$ ,  $e_{k+1}$  is the  $(k+1)$ th (future) estimate,  $i$  is the measured image,  $f$  is the forward projector,  $b$  is the back projector and an asterisk denotes convolution. The PSF is typically used for  $f$ , because  $f$  must accurately account for the blurring imparted by the band-limited microscope.  $b$  is traditionally ‘matched’ to  $f$  as its transpose (that is, by flipping the PSF), but this is not the only possible choice. Work in the field of radiology<sup>14</sup> suggests that using an ‘unmatched’ back projector can accelerate this procedure. Specifically, in the unmatched variant of RLD, iterates were shown to move more rapidly toward desirable reconstructed images when the operator product of the forward projector and back projector had a flatter eigenvalue spectrum. To our knowledge, this result has not been exploited in fluorescence microscopy. When the forward operator is a shift-invariant convolution, as is usually the case in microscopy, the number of iterations can be greatly reduced if  $b$  is chosen so that  $f^* b$  tends toward a delta function (or, equivalently, if the product of the magnitude of the Fourier transforms (FT) of  $f$  and  $b$  approximates a constant in spatial frequency space; Fig. 1 and Supplementary Notes 1–3). To study this effect, we began with images acquired with instant structured illumination microscopy (iSIM)<sup>15</sup>, a super-resolution technique. The iSIM PSF, or  $f$ , resembles a confocal PSF but with smaller spatial extent (Fig. 1a). Although  $b$  is typically chosen to be identical to  $f$  given the transpose symmetry of the iSIM PSF, we considered other choices with progressively smaller spatial extent (or, equivalently, greater amplitude in the spatial frequency passband of the microscope; Fig. 1b and Methods). The last of these was a Butterworth filter designed specifically to ‘invert’ the native iSIM frequency response up to the resolution limit, resulting in a much flatter frequency response of  $|FT(f) \times FT(b)|$  (Fig. 1c). Given its conceptual similarity to a Wiener filter, we termed this choice the ‘Wiener–Butterworth (WB) filter’.

When deconvolving images of 100-nm beads captured with a home-built iSIM, we found that our alternative  $b$  choices produced a resolution-limited result faster than the traditional back projector (Fig. 1d and Supplementary Fig. 1), with a speed-up factor correlating with the constancy of  $|FT(f) \times FT(b)|$ . For example, the WB filter recovered the object’s resolution-limited size with only 1 iteration, whereas the traditional back projector required 15 iterations. The

improved performance of the WB filter did not rely on an improved signal-to-noise ratio (SNR) in the input data (Supplementary Fig. 2), nor did it amplify noise more than other methods (Supplementary Fig. 3). We also compared the WB back projector to the classic Wiener filter employed in noniterative deconvolution. Here too we found that using the WB filter in RLD outperformed the classic Wiener filter (Supplementary Figs. 3 and 4). Butterworth and WB back projectors both introduced unphysical negative values into the deconvolved reconstructions (Fig. 1b and Supplementary Fig. 5). However, because these values were small and typically located within the noise floor of each image, we set them to zero to yield reconstructions that were nearly identical to the conventional RLD results for these and other datasets presented in the paper (Supplementary Tables 1 and 2).

In a simulation, we examined the relative performance of the traditional and WB back projectors in resolving two lines separated by 1.6 times the iSIM resolution limit (Fig. 1e and Supplementary Video 1). Using the same forward operator  $f$  affects the RLD procedure equivalently in both cases, but inspection of the term  $\left[ \frac{i}{e_k^* f} \right]^* b$  reveals that the WB filter applies a much larger ‘correction factor’ to  $e_k$ , accelerating production of the final estimate. Further simulations based on more complex 3D objects confirmed this result, again finding that Gaussian, Butterworth and WB back projectors required fewer iterations to produce deconvolved images with similar (or better) image quality in comparison to traditional RLD (Supplementary Fig. 6 and Supplementary Table 1).

Next, we applied these methods to images of fixed U2OS cells that were immunolabeled to highlight the outer mitochondrial membrane protein Tomm20 and acquired with iSIM (Fig. 1f,g). Each of the back projectors improved signal-to-background and spatial resolution relative to the raw data, better revealing interior voids within the mitochondria. As before, however, using the unmatched back projectors also substantially reduced the number of iterations needed (Supplementary Video 2), a benefit that also extended to time-lapse iSIM (Supplementary Video 3), as well as confocal, wide-field and single-view light-sheet data (Supplementary Fig. 7).

**Accelerating multiview deconvolution and registration.** The more than tenfold improvement in processing speed obtained for single-view deconvolution prompted us to investigate whether our method could also be applied to the more computationally intensive task of multiview deconvolution. We began by applying our method to dual-view light-sheet microscopy (disPIM<sup>9</sup>), using the WB back projector instead of the traditional transpose PSF to perform joint deconvolution on the two registered input views (Methods). As before, the WB back projector produced nearly identical results to the more traditional method, but with only one iteration (Supplementary Fig. 8), a tenfold improvement in speed.

We used our method to reconstruct neuronal dynamics in developing *Caenorhabditis elegans* embryos, obtaining clear images of the plasma membrane of a subgroup of neurons labeled by green fluorescent protein (GFP) in a pan-nuclear mCherry background<sup>16</sup> (Fig. 2a and Supplementary Videos 4 and 5). After deconvolution, the morphologies of neurons and nuclei were sufficiently well resolved (Fig. 2b,c) that we could perform semiautomated lineage<sup>17</sup> to identify neurons selectively labeled by the *fmi-1* promoter in this strain. The anterior OLQVL and OLQVR neurons are glutamatergic sensory neurons that facilitate head foraging and withdrawal reflexes. OLQV neurons are born after their progenitor cells (AB prpaaappa and AB plpaaappa) undergo a terminal cell division to produce OLQVL or OLQVR and sister cells (AB prpaaappap and AB plpaaappap) that undergo programmed cell death<sup>18,19</sup>. The progenitor cells first elaborate broad lamellipodial extensions toward the nose of the animal, which eventually become sensory dendrites (Fig. 2d). Concomitantly with the terminal cell division,

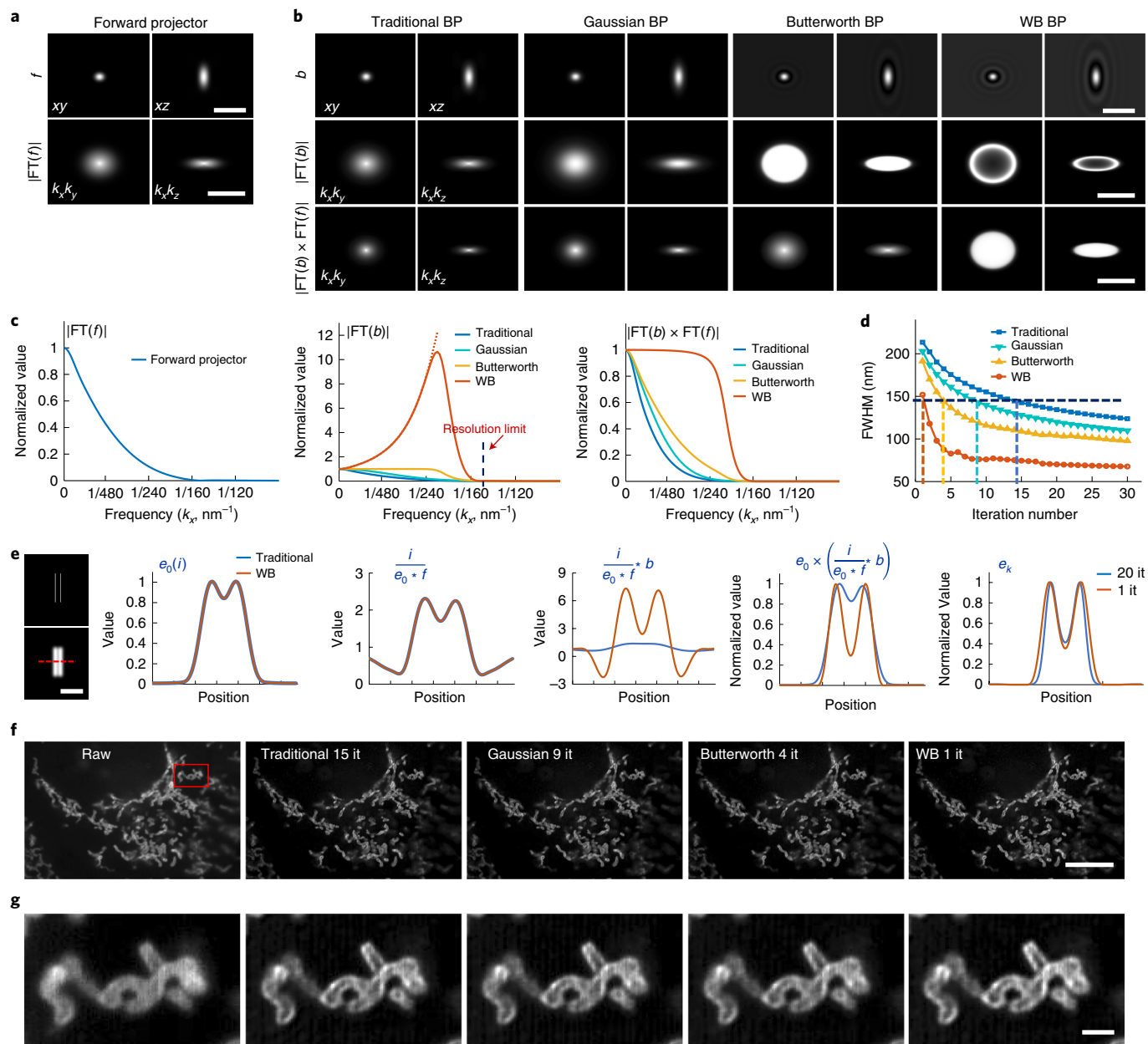


**Fig. 1 | An unmatched back projector reduces the number of iterations required for Richardson-Lucy deconvolution.** **a**, Lateral (left) and axial (right) slices through the forward projector for iSIM, shown in real space (top; PSF) or Fourier space (bottom;  $|FT(f)|$ ). **b**, Different back projectors (BPs), including the traditional back projector (transpose PSF) usually employed in RLD, a Gaussian back projector, a Butterworth back projector and a WB back projector. The first two rows are as in **a**; the last row shows the product of the forward and backward projectors in Fourier space. Note that the color maps for Butterworth and WB PSFs have been adjusted to show the negative values (black rings) that result with these choices and that the color map for the WB Fourier transforms has been adjusted to better show the increase in amplitude at high spatial frequencies. **c**, Line profiles through the Fourier transforms in **a** and **b**, comparing the forward projector (left), back projector (middle) and product of the forward and back projectors (right). The resolution limit of iSIM is indicated by a vertical dashed line in the middle panel. **d**, The apparent size of a 100-nm bead (vertical axis; average FWHM of ten beads after deconvolution) as a function of iteration number (horizontal axis) compared for different back projectors. The resolution limit of iSIM is indicated with a horizontal dashed line. See also Supplementary Fig. 1. **e**, Left, simulated object consisting of two parallel lines in 3D space (top) and the object blurred by the iSIM (bottom). For clarity, only a transverse  $xy$  plane through the object is shown. Right, line profiles corresponding to the red dashed line to the left, comparing the effect of the original (blue) and WB (orange) back projectors in RLD. The estimates after 20 iterations using the original back projector and only 1 iteration using the WB filter are shown in the rightmost graph. **f**, U2OS cells were fixed and immunolabeled to highlight Tomm20, imaged with iSIM and deconvolved. Single planes from imaging stacks are shown, with iteration number and back projector as indicated. **g**, Higher-magnification views, corresponding to the red rectangular region in **f**. See also Supplementary Video 1. Scale bars: 1  $\mu\text{m}$  in top row and 1/100  $\text{nm}^{-1}$  in middle and bottom rows (**a,b**); 1  $\mu\text{m}$  (**e**); 10  $\mu\text{m}$  (**f**); 1  $\mu\text{m}$  (**g**). Experiments were repeated on similar datasets at least three times for **e** and **f**, with similar results obtained each time; representative data from a single experiment are shown.

the lamellipodial extensions become thinner and longer neurites, in line with the final morphological features of the dendrites. Dendrite extension then continues through what appears to be retrograde

extension<sup>20</sup>. Perhaps forces generated during the terminal mitotic division help to create the morphological changes in dendrite shape. Although further experiments are needed to validate this

hypothesis, the form of asymmetric division in which the mother cell does not round up during division and one daughter inherits the shape and polarity of the mother has been described previously in fish<sup>21</sup> and in *C. elegans*<sup>22</sup>. Notably, our reconstructions allowed us to identify single cells in living embryos and to contextualize the morphological changes undergone by neurons during terminal cell divisions leading to dendrite biogenesis.

Our methods extend to imaging configurations with more views. For example, we acquired a quadruple-view dataset on a triple-objective light-sheet microscope<sup>11</sup> (Fig. 2e, Supplementary Fig. 9 and Supplementary Video 6). E6-1 Jurkat T cells stably transfected to express EGFP–actin were plated on coverslips coated with anti-CD3 antibodies (mimicking antigen-presenting cells). After the T cells spread on the coverslip, we imaged them for 30 time points (one time point every 15 s) spanning 7.5 min, acquiring four volumetric views at each time point. After adapting our deconvolution method for this acquisition scheme (Methods), dynamic changes in membrane ruffles and cell protrusions were obvious in the reconstructions (Fig. 2f), but were obscured in the raw data (Supplementary Fig. 10). Using the WB back projector reduced the number of iterations from 90 to 5 (Fig. 2g). Notably, our method also outperformed the state-of-the-art efficient Bayesian multiview deconvolution (EBMD)<sup>10</sup> method (which required 30 iterations to produce images of similar quality), which can be explained by the flatter frequency response of  $|FT(f) \times FT(b)|$  when using the WB filter in comparison to the EBMD result (Supplementary Fig. 11).

In processing these dual- and quadruple-view datasets, we noticed that the time for image registration considerably exceeded the time for deconvolution, usually by 75- to 120-fold. One approach to faster image registration encases the sample in a labeled matrix,

using the multiple feature points from many fiducials to obtain the registration among different views<sup>23</sup>. We opted instead for the less invasive option of greatly accelerating the speed of our image-based registration software. First, we rewrote our CPU-based registration code<sup>9</sup> in CUDA so that the procedure could be run entirely on our GPU. Second, we improved the underlying registration algorithm by incorporating an initial two-dimensional (2D) registration and progressively more complex 3D registrations, which resulted in faster and more robust performance (Fig. 2h, Supplementary Fig. 12, Methods and Supplementary Software). Collectively, these advances resulted in 175- and 30-fold speed-ups in registration (Fig. 2i), respectively, for the modestly sized *C. elegans* and T cell datasets presented in Fig. 2a,e, which enabled total processing times on par with the acquisition time (Supplementary Table 3). We also benchmarked our improved registration method against established registration tools, including elastix<sup>24</sup> and NiftyReg<sup>25</sup>. In comparison to these state-of-the-art tools, our method enabled a speed improvement of more than tenfold on large volumetric light-sheet datasets without sacrificing registration quality (Supplementary Table 4).

Our improved registration method enabled an even more dramatic speed-up (451-fold; Fig. 2i) for an extended DISPIM acquisition spanning 900 volumes (7.5 h, 1.05 teravoxels, 2.1 TB), where we followed the migration of the lateral line primordium in a 32-h zebrafish embryo expressing Lyn-eGFP under the control of the claudin B (*cldnb*) promoter<sup>26</sup> (Fig. 2j and Supplementary Video 7). Following registration, joint WB deconvolution improved visualization of vesicular structures and cell boundaries as compared to the raw data (Fig. 2k,l) and facilitated inspection of dynamic immune cells that appeared to migrate between the skin and underlying somites (Fig. 2m,n and Supplementary Video 8). WB deconvolution

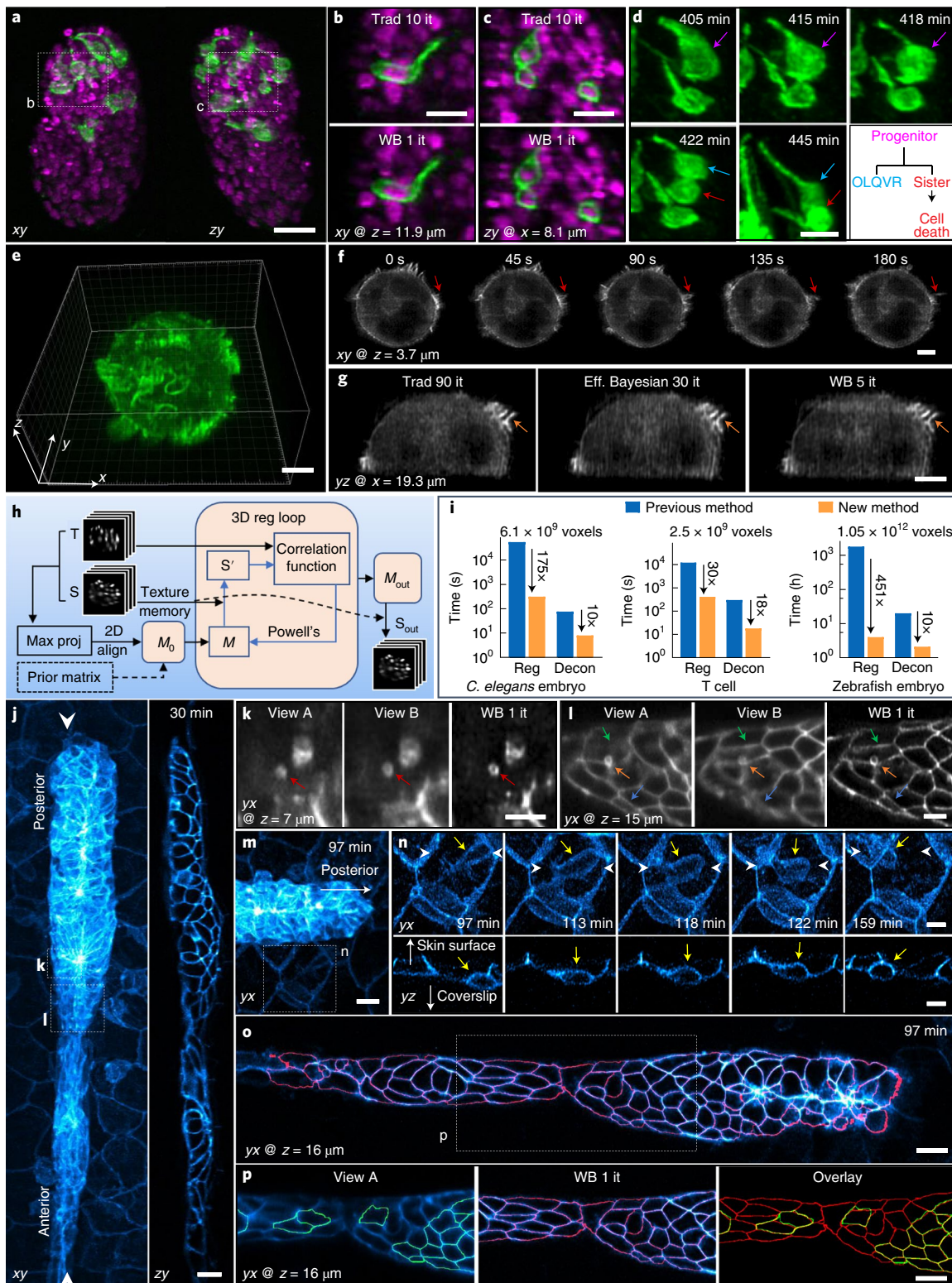
**Fig. 2 | Improvements in deconvolution and registration accelerate the processing of multiview light-sheet datasets.** **a**, Lateral (left) and axial (right) maximum-intensity projections demonstrating isotropic reconstructions of *C. elegans* embryos expressing neuronal (green, GFP-membrane marker) and pan-nuclear (magenta, mCherry-histone) markers. Images were captured with diSPIM, and deconvolution was performed using the WB filter. See also Supplementary Video 4. **b,c**, Higher-magnification single slices from the dashed rectangular regions in **a**, emphasizing the similarity between reconstructions obtained with traditional RLD ('trad') and WB deconvolution. The number of iterations for each method is displayed. **d**, Higher-magnification maximum-intensity projection view of neuronal dynamics, indicating neurite extension and terminal cell division, for a progenitor cell (purple arrow), OLQVR cell (blue arrow) and apoptotic sister cell (red arrow). See also the lower right schematic and Supplementary Video 5. **e**, WB reconstruction of a Jurkat T cell expressing EGFP–actin; raw data were captured in a quadruple-view light-sheet microscope. **f**, Selected slices 3.7 μm from the coverslip surface. Indicated time points display fine actin dynamics at the cell periphery (red arrows). See also Supplementary Video 6. **g**, Axial slice through the sample, indicating close similarity (orange arrows) between traditional, efficient Bayesian and WB deconvolution with the iteration number as indicated. **h**, Schematic of the GPU-based 3D registration used for multiview fusion. Example inputs are two 3D images, referred to as the source (*S*; image to be registered) and target (*T*; fixed image) images. Maximum-intensity projections of the input 3D images are used for preliminary alignment and to generate an initial transformation matrix ( $M_0$ ). Alternatively, a transformation matrix from a previous time point is used as  $M_0$ . A 3D registration loop iteratively performs affine transformations on the source image (which is kept in GPU texture memory for fast interpolation), using Powell's method for updating the transformation matrix by minimizing the correlation ratio between the transformed source image (*S'*) and the target image. **i**, Bar graphs showing the time required to process the datasets (file I/O not included) in this figure (left, middle and right columns correspond to the datasets in **a**, **e** and **j**, respectively, with voxel count as indicated) conventionally and with our new methods. The conventional registration method was performed with an existing MIPAV plugin (Methods) using CPUs, while the new registration method was performed using GPUs. Both deconvolution methods were performed with GPUs. Note the log scale on the ordinate and that the listed times apply for the entire time series in each case (the total time for the conventional registration method on the zebrafish dataset was extrapolated from the time required to register ten time points). **j**, Representative lateral (left, maximum-intensity projection) and axial (right, single plane corresponding to the white arrowheads in the left panel) images showing a 32-h zebrafish embryo expressing Lyn-eGFP under the control of the claudin B (*cldnb*) promoter, marking cell boundaries within and outside the lateral line primordium. Images were captured with diSPIM; WB reconstructions are shown. Images were selected from the volume 30 min into the acquisition; see also Supplementary Video 7. **k,l**, Higher-magnification views of the dashed rectangles in **j**, emphasizing improvement in resolving vesicles (red and orange arrows) and cell boundaries (green and blue arrows) with WB deconvolution as compared to raw data. Note that **k** and **l** are rotated 90 degrees relative to **j**. **m**, Higher-magnification view of the leading edge of the lateral line, 97 min into the acquisition. **n**, Higher-magnification view of the dashed rectangular region in **m**, emphasizing immune cell (yellow arrows) migration between surrounding skin cells. White arrowheads are provided to give context, and white arrows point to the skin surface and coverslip. Top row, maximum-intensity projection of the lateral view; bottom row, single plane of the axial view. See also Supplementary Video 8. **o**, Lateral slice through the primordium, with automatically segmented cell boundaries marked in red. See also Supplementary Video 9. **p**, Higher-magnification view of the dashed rectangle in **o**, showing differential segmentation with raw single-view data (green, left) versus deconvolved data (red, middle). The overlay to the right shows common segmentations (yellow) versus segmentations found only in the deconvolved data (red). Note that the 'z' coordinate in **j–p** is defined normal to the coverslip surface. Scale bars: 10 μm (**a,m,o,p**); 5 μm (all other panels). Experiments were repeated on similar datasets at least three times for **a–d** and two times for **e–g** and **j–p**, with similar results obtained each time; representative data from a single experiment are shown.

also substantially improved automated segmentation of cells within the lateral line, as only 71 of 120 cells were accurately segmented in the raw data versus 116 of 120 in the deconvolved data (Fig. 2o,p and Supplementary Video 9).

We also tested our methods on single-view and multiview datasets acquired with a commercial Zeiss Lightsheet Z.1 microscope (Supplementary Figs. 13 and 14, Supplementary Video 10 and Methods), obtaining improved resolution and contrast after decon-

volution and improved speed in comparison to the widely used commercial Huygens deconvolution software (Supplementary Fig. 13, Supplementary Table 3 and Methods).

**Submicrometer isotropic imaging of large cleared-tissue volumes.** Other samples that benefit from improved multiview fusion and deconvolution are large volumes of cleared tissue, which can be rapidly imaged using light-sheet microscopes. To explore this



possibility, we constructed a cleared-tissue diSPIM (Supplementary Fig. 15), replacing our original water-immersion objectives with a pair of mixed-immersion  $\times 17.9$ , 0.4-numerical aperture (NA) objectives (Methods). To estimate spatial resolution, we imaged 100-nm fluorescent beads in dibenzyl ether (Sigma, 108014), obtaining a single-view lateral full width at half maximum value (FWHM) of  $0.84 \pm 0.04 \mu\text{m}$  and an axial FWHM of  $4.6 \pm 0.4 \mu\text{m}$  (ten beads, mean  $\pm$  s.d.; Supplementary Fig. 16). Registration and one iteration of WB deconvolution further improved spatial resolution, resulting in an isotropic  $0.79 \pm 0.04 \mu\text{m}$ , offering a several-fold improvement in axial resolution over previous single-view experiments using the same lens<sup>27,28</sup>. Next, we fixed, cleared and immunolabeled millimeter-scale samples of mouse tissue (Fig. 3a–d and Supplementary Videos 11–15) with iDISCO+ (ref. <sup>29</sup>) or iDISCO<sup>30</sup>, subsequently imaging them with the cleared-tissue diSPIM in stage scanning mode<sup>31</sup>.

The resulting data span hundreds of gigavoxels to teravoxels, up to  $\sim 2$  TB in size. This size presents a major challenge, as such whole raw views do not fit within the memory of single GPU cards and must be subdivided before processing. To address this challenge, we created a processing pipeline for terabyte-scale data: cropping the single-view data into subvolumes, registering and deconvolving the subvolumes, and finally stitching the resulting reconstructions back into a higher-resolution composite (Supplementary Figs. 17 and 18).

In a first example, we imaged a  $4 \times 2 \times 0.5 \text{ mm}^3$  slab of brain tissue derived from a V1b-transgenic mouse<sup>32</sup>, with sparse immunolabeling of neurons and neurites across the entire volume (Fig. 3a). The isotropic resolution of the deconvolved reconstruction enabled us to resolve individual neurites at the micrometer scale (Fig. 3a) and to observe fine detail laterally and axially that was not resolved in the raw data (Fig. 3b). Manual tracing of neurites was also substantially improved in the deconvolved data relative to the raw data (Fig. 3c). In a second example, we performed four-color imaging on the gut of an embryonic day (E) 18.5 mouse, spanning a  $2.1 \times 2.5 \times 1.5 \text{ mm}^3$  volume (Fig. 3d). Our reconstruction highlights the organized and hierarchical structure of the intestine, including the interconnected vascular plexus feeding the submucosal and mucosal intestinal areas (PECAM-1 and DAPI staining), mitochondrially enriched regions within the mucosa (Tomm20 and DAPI staining) and tubulin-dense regions within the outer

intestinal wall ( $\alpha$ -tubulin and PECAM-1 staining). As with the brain sample, the isotropic submicrometer-scale resolution allowed us to visualize fine details that were otherwise obscured by diffraction, including hollow blood vessels and cytoplasmic mitochondria surrounding individual nuclei (Supplementary Fig. 19). Notably, obtaining these as well as other large reconstructions of mouse intestine, stomach and ovary datasets (Supplementary Videos 13–15 and Supplementary Tables 5 and 6) was facilitated by our much faster postprocessing methods. Collectively, the new registration (Fig. 2h) and deconvolution (Fig. 1) methods account for a 100-fold speed improvement over previous efforts, enabling postprocessing in tens of hours rather than tens of days (Fig. 3e). We note that our method delivers less light dose than a recent technique with similar reported resolution<sup>33</sup>, as our technique confines the illumination to the vicinity of the focal plane.

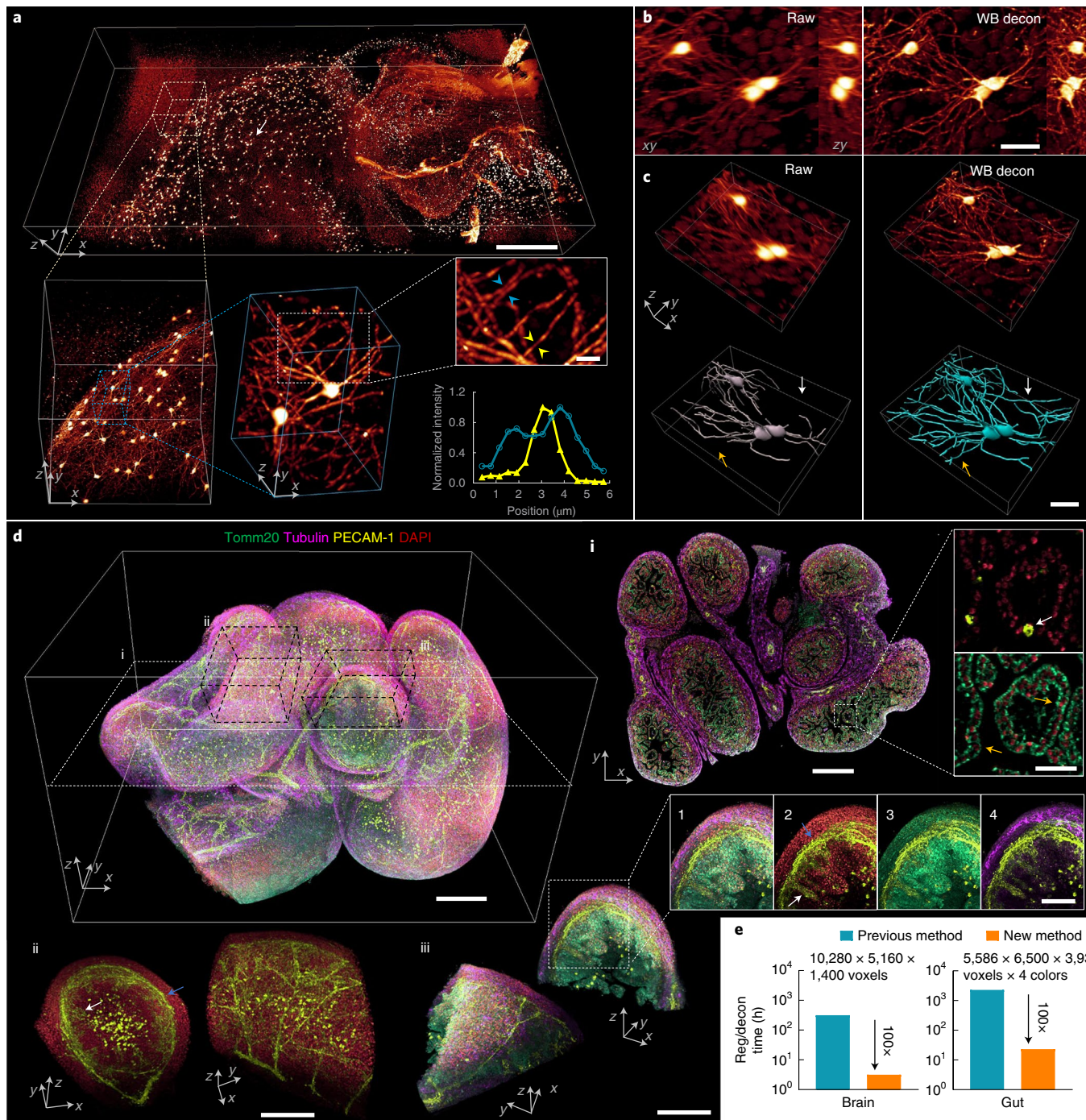
**Accelerating deconvolution with a spatially varying PSF.** Finally, we developed methods for accelerating the deconvolution of fluorescence microscopy data blurred with a spatially varying PSF, acquired by imaging samples deposited on reflective coverslips (Fig. 4 and Supplementary Table 7). As we previously demonstrated<sup>13</sup>, reflective diSPIM enables the collection of additional specimen views (Fig. 4a), increasing information content and boosting spatio-temporal resolution. However, the raw reflective data are contaminated by substantial epifluorescence that varies over the imaging field (Fig. 4c). To remove the epifluorescence and fuse the views for optimal resolution enhancement, registration and subsequent deconvolution with a spatially varying PSF are needed (Methods). Unfortunately, spatially varying deconvolution carries a considerable computational burden: as applied to reflective imaging, it requires calculation of the forward and back projectors at each axial slice instead of only once per volume<sup>13</sup>. For example, deconvolving an imaging volume spanning  $340 \times 310 \times 340$  voxels with 20 iterations of traditional RLD with a spatially varying PSF requires  $340 \text{ slices} \times 2 \text{ views} \times 2 \text{ convolutions per RL update} \times 20 \text{ iterations} = 27,200$  3D convolutions (14 min per volume with a single GPU card), instead of the  $2 \times 2 \times 20$  iterations = 80 3D convolutions required with a spatially invariant PSF (only 2.5 s per volume). Unlike in our previous examples (Figs. 2 and 3), deconvolution rather than registration becomes the bottleneck in postprocessing the raw data.

**Fig. 3 | Imaging millimeter-scale cleared-tissue volumes with isotropic micrometer-scale spatial resolution.** **a**, Brain volume of  $4 \times 2 \times 0.5 \text{ mm}^3$  from fixed and iDISCO+-cleared V1b mouse, immunolabeled with Alexa Fluor 555-conjugated secondary antibody against anti-tdTomato primary antibody, imaged with cleared-tissue diSPIM and reconstructed after dual-view registration and WB deconvolution. Progressively higher-resolution subvolumes are shown, with line profiles indicating neurite FWHM of  $1.3 \mu\text{m}$  (yellow arrowheads) and separation of  $1.9 \mu\text{m}$  between neurites (blue arrowheads). See also Supplementary Video 11. **b**, Lateral and axial cross-sections from the region indicated with a white arrow in **a**, emphasizing the higher resolution obtained with WB deconvolution (decon) as compared to raw single-view data. **c**, Volume renderings of the region displayed in **b**, again comparing raw data to deconvolution. Manually traced neurites are shown in the bottom row; colored arrows indicate neurites traced in deconvolution that are obscured in raw single-view data. **d**, Intestinal volume of  $2.1 \times 2.5 \times 1.5 \text{ mm}^3$  from fixed and iDISCO-cleared E18.5 mouse labeled with DAPI (red), Alexa Fluor 647-conjugated secondary antibody against anti-Tomm20 primary antibody (green), Alexa Fluor 488-conjugated secondary antibody against anti-PECAM-1 primary antibody (yellow) and Alexa Fluor 568-conjugated secondary antibody against anti- $\alpha$ -tubulin primary antibody (purple); imaged with cleared-tissue diSPIM; and reconstructed after dual-view registration and WB deconvolution. See also Supplementary Video 12. **i**, Single plane demarcated by the dashed white rectangular region at left, showing a four-color cross-section and higher-magnification dual-color views highlighting a hollow blood vessel (white arrow) and mitochondria surrounding individual nuclei (orange arrows). **ii**, Subvolume demarcated by the dashed black parallelepiped above, illustrating different perspectives of the vascular plexus supplying the submucosa (blue arrow) and mucosa (white arrow) of the intestine. **iii**, Different perspectives of the four-color subvolume demarcated by the dashed black parallelepiped above and insets 1–4, highlighting hierarchical organization within the intestine, for example, submucosa (blue arrow) and mucosa (white arrow) (inset 2); mitochondrially enriched regions that support the high energy demand and constant cellular renewal within the mucosa (inset 3); and outer intestinal wall with dense  $\alpha$ -tubulin staining (inset 4). See also Supplementary Fig. 19. **e**, Bar graphs showing the registration and deconvolution time required for postprocessing datasets (image sizes in **a** and **d** as indicated), comparing previous (blue) and new (orange; 100-fold reduction in time) postprocessing methods. Note that times for the previous method are estimated (see Methods for further detail) and the log scale on the ordinate axes. Scale bars:  $500 \mu\text{m}$ ,  $100 \mu\text{m}$ ,  $30 \mu\text{m}$  and  $10 \mu\text{m}$  for progressively higher magnifications (**a**);  $30 \mu\text{m}$  (**b**, **c**);  $300 \mu\text{m}$  in top left,  $300 \mu\text{m}$  and  $30 \mu\text{m}$  for insets in **i**,  $200 \mu\text{m}$  in **ii**, and  $200 \mu\text{m}$  and  $100 \mu\text{m}$  for insets in **iii** (**d**). See also Supplementary Videos 13–15. Experiments were repeated on similar datasets at least three times, with similar results obtained each time; representative data from a single experiment are shown.

By modifying the spatially varying RL update to incorporate the WB filter (Methods), we found that only two iterations were required to deconvolve a previously published dataset<sup>13</sup> highlighting calcium waves (marked with GCaMP3) within muscles in threefold-stage *C. elegans* embryos. As with traditional RLD, the WB modification improved contrast and resolution in the raw data (Fig. 4c and Supplementary Video 16), but with a tenfold reduction in processing time (Fig. 4h). These gains also extended to a new form of reflective microscopy, using a higher-NA LLS microscope instead of diSPIM (Fig. 4a,d–f,i and Methods).

LLS microscopy<sup>34</sup> has garnered attention owing to its combination of high detection NA and illumination structure; together, these attributes result in a better compromise between field-of-view

and light-sheet thickness than with previous microscopes using pseudo-non-diffracting beams. Nevertheless, the contrast and spatial resolution in raw LLS images still suffer from extraneous out-of-focus light owing to illumination sidelobes, an effect that can be ameliorated with deconvolution. We found that the performance of the base LLS microscope could be further improved by imaging samples deposited on reflective coverslips (Fig. 4d–f), registering the two resulting high-NA views oriented ~113 degrees apart and deconvolving them with a spatially varying PSF. As assayed with images of immunolabeled microtubules in U2OS cells captured on glass (Fig. 4d) and reflective (Fig. 4e) coverslips, axial resolution was improved twofold, from  $750 \pm 39$  nm to  $379 \pm 23$  nm (Supplementary Fig. 20). Deconvolving registered images of mEmerald- $\alpha$ -actinin in



live U2OS cells acquired in the reflective LLS microscope with the WB filter instead of traditional RLD resulted in a 15-fold reduction in processing time (Fig. 4*i* and Supplementary Video 17).

While a 10- to 15-fold reduction in processing time is substantial, the time associated with deconvolution still far exceeds the time needed for data acquisition (3.5 h to deconvolve the 150-volume *C. elegans* dataset imaged with reflective diSPIM; 13.3 h to deconvolve the 100-volume  $\alpha$ -actinin dataset imaged with reflective LLS microscopy). To obtain further speed enhancements, we turned to deep learning<sup>35</sup>, which has resurged as a promising framework for image classification<sup>36</sup>, image recognition<sup>37</sup>, image segmentation<sup>38</sup>, denoising<sup>39</sup>, super-resolution<sup>40</sup> and deconvolution<sup>41</sup>.

We constructed a convolutional neural network, terming it ‘DenseDeconNet’, as it is based on linking together dense network blocks<sup>42</sup> in a memory-efficient manner (Fig. 4**b**, Supplementary Note 4 and Supplementary Software). These blocks use multiple dense connections to extract features from the raw image stacks and then learn to deblur the images. Unlike previous attempts that deblur 2D image slices by comparing the data to synthetically blurred slices and average the network output from two orthogonal views to improve resolution isotropy<sup>43</sup>, we designed our method to operate on the full volumetric data, thereby learning the requisite 3D restoration directly. This capability is especially important in reflective applications, in which a simple 2D spatially invariant blur cannot properly model the physics of the microscope.

We began by testing DenseDeconNet on nuclear and membrane-bound labels expressed in live *C. elegans* embryos, acquired on the diSPIM using conventional glass coverslips. We used the deconvolved dual-view data as ground truth. When using only a single view as the input to the network, DenseDeconNet provided resolution enhancement intermediate between the raw data and the deconvolved result (Supplementary Video 18). To some extent, this is unsurprising; presumably only with both views is there enough information to recover the isotropic resolution provided by diSPIM. However, for highly dynamic structures, the network output with a single-view input sometimes provided more accurate reconstructions than the deconvolved ground truth (Supplementary Note 4). We suspect this result is due to the lessened effect of motion blur, which otherwise causes errors in both registration and deconvolution. Additionally, in

bypassing registration, the DenseDeconNet with single-view input provided a fivefold reduction in total processing time as compared to WB deconvolution, that is, ~1 s for application of DenseDeconNet versus 5 s for the new registration method (Fig. 2*h*) and one iteration of WB deconvolution (Supplementary Note 4).

Using both registered views for network input enabled resolution enhancement very similar to the ground-truth joint deconvolution on data acquired with glass coverslips (Supplementary Note 4). This result also extended to the reflective datasets. When training the network using the raw specimen views as inputs and the WB result as the ground truth, DenseDeconNet produced outputs that were nearly identical to the ground truth (based on visual inspection; Fig. 4*c,f*; mean square error (MSE) of  $4.8 \times 10^{-4}$  (Fig. 4*c*) and  $5.0 \times 10^{-5}$  (Fig. 4*f*) and structural similarity (SSIM) index of 0.923 (Fig. 4*c*) and 0.965 (Fig. 4*f*), resulting in clear images of calcium dynamics in embryonic muscle (Supplementary Video 16) and  $\alpha$ -actinin dynamics at the cell boundary (Fig. 4*g* and Supplementary Video 17). Notably, the network output offered a 50-fold speed improvement over WB deconvolution (1.68 s per volume, or a 500-fold improvement over traditional RLD) when processing the *C. elegans* data (Fig. 4*h*) and a 160-fold speed improvement (2 s per volume, or a 2,400-fold improvement over traditional RLD) when processing the  $\alpha$ -actinin data (Fig. 4*i* and Supplementary Table 7).

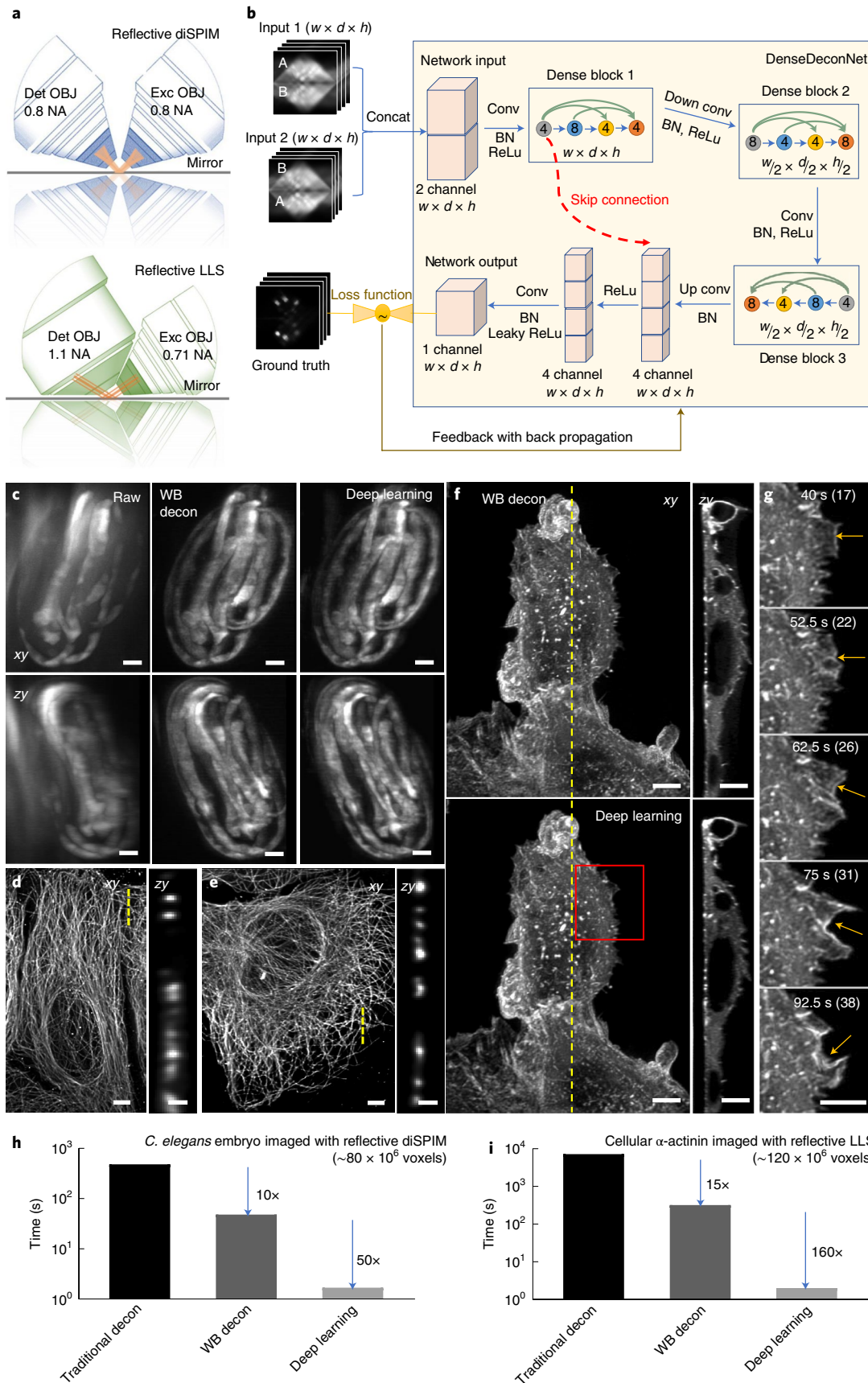
## Discussion

Our deconvolution method is inspired by RLD but achieves high-quality reconstructions more rapidly. Although the WB filter indeed enables deconvolution with fewer iterations than a traditional back projector, the potential to introduce artifacts still exists, particularly if too many iterations are applied (Fig. 1*d* and Supplementary Fig. 6). We recommend a single iteration as a good rule of thumb, because this choice resulted in resolution-limited performance on the majority of the datasets we examined (Table 2.1 in Supplementary Note 2). With this caveat in mind, the algorithmic improvements we describe here should accelerate image-based biological discovery, especially for the increasingly rich and large datasets that can be obtained with modern light microscopes. For raw data that fit within the memory of a single GPU card (Figs. 1, 2 and 4), our methods now enable multiview registration and

**Fig. 4 | Deep learning massively accelerates deconvolution with a spatially varying PSF.** **a**, Reflective imaging geometries for a diSPIM (top) and LLS (bottom) microscope. In both cases, the sample is deposited on a reflective coverslip (mirror), which produces additional views of the specimen. Det OBJ, detection objective; Exc OBJ, excitation objective. **b**, Schematic architecture of our convolutional neural network (DenseDeconNet) used for deep learning. Inputs are concatenated ('Concat') image volumes (each containing width (*w*)  $\times$  depth (*d*)  $\times$  height (*h*) voxels) obtained from the microscope, which may contain multiple views (A, B) of the specimen. Three 'dense blocks' extract feature maps (circles) from the network input, eventually learning to reverse the spatially varying blurring imparted by the microscope by minimizing the difference (loss function) between the network output and the ground-truth reconstruction via back propagation. Conv, convolution; BN, batch normalization; ReLu, rectified linear unit. Circles within each dense block unit show the number of feature maps after each convolutional layer; colored arrows within each dense block show the concatenation of successive layers in the network. See Supplementary Note 4 for more details on the network architecture. **c**, Threefold *C. elegans* embryos expressing GCaMP3 from a myo-3 promoter were imaged by reflective diSPIM (150 volumes, each acquired every 350 ms). Maximum-intensity projections of raw data (left), WB deconvolution (middle) and deep learning reconstruction (right) are shown for lateral (top) and axial (bottom) views. See also Supplementary Video 16. **d**, U2OS cells were deposited on glass coverslips and fixed, microtubules were immunolabeled with anti- $\alpha$ -tubulin conjugated to Alexa Fluor 488, and cells were imaged with LLS microscopy. A lateral maximum-intensity projection (left) and axial slice (right; corresponding to the yellow dashed line at left) are shown. **e**, U2OS cells were deposited on reflective coverslips and fixed, immunolabeled and imaged as in **d**. A lateral maximum-intensity projection (left) and axial slice (right; corresponding to the yellow dashed line at left) are shown. Reconstructions in **d** and **e** were performed using traditional deconvolution with a spatially varying PSF. See also Supplementary Fig. 20. **f**, U2OS cells expressing mEmerald- $\alpha$ -actinin were deposited on reflective coverslips and imaged (100 volumes, each acquired every 2.5 s) in the LLS microscope. Reconstructions were performed via WB deconvolution (top) and deep learning (bottom). A lateral maximum-intensity projection (left) and axial slice (right; corresponding to the yellow dashed line at left) are shown. See also Supplementary Video 17. **g**, Higher-magnification view of the red rectangular region, emphasizing the dynamics of  $\alpha$ -actinin near the cell boundary (yellow arrows). **h,i**, Bar graphs showing the time required for processing of a single volume using traditional deconvolution with a spatially varying PSF, deconvolution via the WB filter and deep learning for the dataset shown in **c** (**h**) and the dataset shown in **f** (**i**). Note the log scale on the ordinate. Note also that the time cost of file I/O is not included in **h** and **i**. Scale bars: 5  $\mu$ m in all panels except 1  $\mu$ m in the zy views in **d** and **e**. For **c-i**, traditional and WB deconvolution experiments were repeated on similar datasets at least two times, with similar results obtained each time; the deep learning model was trained on one time-lapse dataset and applied to multiple datasets ( $N \geq 2$ ), with similar results obtained for each dataset.

deconvolution on a timescale on par with, and frequently faster than, image acquisition. For much larger multiview light-sheet datasets (Fig. 3), our approach drastically shortens the postprocessing time necessary for image reconstruction, instead placing the bottleneck

on file reading, file writing and image stitching (Supplementary Table 5). Further speed improvements are possible if these operations are optimized. Alternatively, compressing the image data or using multiple graphics cards for additional parallelization<sup>12</sup> could



further shorten postprocessing time. We freely provide our software (Supplementary Software) in the hope that others may improve it and expect that other multiview light-sheet<sup>12</sup> (Supplementary Fig. 14) or light-field configurations<sup>44</sup> could benefit from our work.

When performing deconvolution with a spatially varying PSF, the WB method provides a substantial speed-up over traditional RLD, yet we obtained an even greater acceleration with deep learning. We note several caveats, however, when using deep learning methods. First, enough high-quality training data (for our network, ~50–100 training pairs) must be accumulated before application of the network, underscoring the point that deep learning augments, but does not replace, more classic deconvolution. Second, although application of the trained network takes only seconds per volume, training the network still takes days on a single graphics card. Finally, the networks are ‘brittle’; we obtained optimal results by retraining the network on each new sample (Supplementary Note 4). Designing more general neural networks remains an important area for further research.

## Online content

Any methods, additional references, Nature Research reporting summaries, source data, extended data, supplementary information, acknowledgements, peer review information; details of author contributions and competing interests; and statements of data and code availability are available at <https://doi.org/10.1038/s41587-020-0560-x>.

Received: 25 September 2019; Accepted: 15 May 2020;

Published online: 29 June 2020

## References

- Barrett, H. H. & Myers, K. J. *Foundations of Image Science* (John Wiley and Sons, 2004).
- Sarder, P. & Nehorai, A. Deconvolution methods for 3-D fluorescence microscopy images. *IEEE Signal Process. Mag.* **23**, 32–45 (2006).
- Richardson, W. H. Bayesian-based iterative method of image restoration. *J. Opt. Soc. Am.* **62**, 55–59 (1972).
- Lucy, L. B. An iterative technique for the rectification of observed distributions. *Astron. J.* **79**, 745–754 (1974).
- Ingaramo, M. et al. Richardson–Lucy deconvolution as a general tool for combining images with complementary strengths. *ChemPhysChem* **15**, 794–800 (2014).
- Gustafsson, M. G. L. Surpassing the lateral resolution limit by a factor of two using structured illumination microscopy. *J. Microsc.* **198**, 82–87 (2000).
- Wu, Y. & Shroff, H. Faster, sharper, and deeper: structured illumination microscopy for biological imaging. *Nat. Methods* **15**, 1011–1019 (2018).
- Temerinac-Ott, M. et al. Multiview deblurring for 3-D images from light-sheet-based fluorescence microscopy. *IEEE Trans. Image Process.* **21**, 1863–1873 (2012).
- Wu, Y. et al. Spatially isotropic four-dimensional imaging with dual-view plane illumination microscopy. *Nat. Biotechnol.* **31**, 1032–1038 (2013).
- Preibisch, S. et al. Efficient Bayesian-based multiview deconvolution. *Nat. Methods* **11**, 645–648 (2014).
- Wu, Y. et al. Simultaneous multiview capture and fusion improves spatial resolution in wide-field and light-sheet microscopy. *Optica* **3**, 897–910 (2016).
- Chhetri, R. K. et al. Whole-animal functional and developmental imaging with isotropic spatial resolution. *Nat. Methods* **12**, 1171–1178 (2015).
- Wu, Y. et al. Reflective imaging improves spatiotemporal resolution and collection efficiency in light sheet microscopy. *Nat. Commun.* **8**, 1452 (2017).
- Zeng, G. L. & Gullberg, G. T. Unmatched projector/backprojector pairs in an iterative reconstruction algorithm. *IEEE Trans. Med. Imaging* **19**, 548–555 (2000).
- York, A. G. et al. Instant super-resolution imaging in live cells and embryos via analog image processing. *Nat. Methods* **10**, 1122–1126 (2013).
- Walton, T. et al. The *Bicoid* class homeodomain factors *ceh-36/OTX* and *unc-30/PTX* cooperate in *C. elegans* embryonic progenitor cells to regulate robust development. *PLoS Biol.* **11**, e1005003 (2015).
- Bao, Z. et al. Automated cell lineage tracing in *Caenorhabditis elegans*. *Proc. Natl Acad. Sci. USA* **103**, 2707–2712 (2006).
- Yamaguchi, Y. & Miura, M. Programmed cell death in neurodevelopment. *Dev. Cell* **32**, 478–490 (2015).
- Yeo, W. & Gautier, J. Early neural cell death: dying to become neurons. *Dev. Biol.* **274**, 233–244 (2004).
- Heiman, M. G. & Shaham, S. DEX-1 and DYF-7 establish sensory dendrite length by anchoring dendritic tips during cell migration. *Cell* **137**, 344–355 (2009).
- Costa, G. et al. Asymmetric division coordinates collective cell migration in angiogenesis. *Nat. Cell Biol.* **18**, 1292–1301 (2016).
- Shah, P. K. et al. An *in toto* approach to dissecting cellular interactions in complex tissues. *Dev. Cell* **43**, 530–540 (2017).
- Preibisch, S., Saalfeld, S., Schindelin, J. & Tomancak, P. Software for bead-based registration of selective plane illumination microscopy data. *Nat. Methods* **7**, 418–419 (2010).
- Klein, S., Staring, M., Murphy, K., Viergever, M. A. & Pluim, J. P. W. elastix: a toolbox for intensity based medical image registration. *IEEE Trans. Med. Imaging* **29**, 196–205 (2010).
- Modat, M. et al. Global image registration using a symmetric block-matching approach. *J. Med. Imaging* **1**, 024003 (2014).
- Haas, P. & Gilmour, D. Chemokine signaling mediates self-organizing tissue migration in the zebrafish lateral line. *Dev. Cell* **10**, 673–680 (2006).
- Nicovich, P. R. et al. Multimodal cell type correspondence by intersectional mFISH in intact tissues. Preprint at *bioRxiv* <https://doi.org/10.1101/525451> (2019).
- Glaser, A. K. et al. Multi-immersion open-top light-sheet microscope for high-throughput imaging of cleared tissues. *Nat. Commun.* **10**, 1–8 (2019).
- Renier, N. et al. Mapping of brain activity by automated volume analysis of immediate early genes. *Cell* **165**, 1789–1802 (2016).
- Renier, N. et al. iDISCO: a simple, rapid method to immunolabel large tissue samples for volume imaging. *Cell* **159**, 896–910 (2014).
- Kumar, A. et al. Using stage- and slit-scanning to improve contrast and optical sectioning in dual-view inverted light-sheet microscopy (diSPIM). *Biol. Bull.* **231**, 26–39 (2016).
- Avram, S. K. W. et al. NMDA receptor in vasopressin 1b neurons is not required for short-term social memory, object memory or aggression. *Front. Behav. Neurosci.* **13**, 218 (2019).
- Chakraborty, T. et al. Light-sheet microscopy with isotropic, sub-micron resolution and solvent-independent large-scale imaging. Preprint at *bioRxiv* <https://doi.org/10.1101/605493> (2019).
- Chen, B. C. et al. Lattice light-sheet microscopy: imaging molecules to embryos at high spatiotemporal resolution. *Science* **346**, 1257998 (2014).
- LeCun, Y., Bengio, Y. & Hinton, G. Deep learning. *Nature* **521**, 436–444 (2015).
- Krizhevsky, A., Sutskever, I. & Hinton, G. ImageNet classification with deep convolutional neural networks. In *Advances in Neural Information Processing Systems 25* (eds. Pereira, F. et al.) 1097–1105 (Curran Associates, 2012).
- He, K., Zhang, X., Ren, S. & Sun, J. Deep residual learning for image recognition. In *IEEE Conference on Computer Vision and Pattern Recognition* 770–778 (IEEE, 2016).
- Girshick, R. B., Donahue, J., Darrell, T. & Malik, J. Rich feature hierarchies for accurate object detection and semantic segmentation. In *IEEE Conference on Computer Vision and Pattern Recognition* 580–587 (IEEE, 2014).
- Xie, J., Xu, L. & Chen, E. Image denoising and inpainting with deep neural networks. In *Advances in Neural Information Processing Systems 25* (eds. Pereira, F. et al.) 341–349 (Curran Associates, 2012).
- Dong, C., Loy, C. C., He, K. & Tang, X. Image super-resolution using deep convolutional networks. *IEEE Trans. Pattern Anal. Mach. Intell.* **38**, 295–307 (2015).
- Xu, L., Ren, J. S., Liu, C. & Jia, J. Deep convolutional neural network for image deconvolution. In *Advances in Neural Information Processing Systems 27* (eds. Ghahramani, Z. et al.) 1790–1798 (Curran Associates, 2014).
- Huang, G., Liu, Z., van der Maaten, L. & Weinberger, K. Q. Densely connected convolutional networks. In *IEEE Conference on Computer Vision and Pattern Recognition* 4700–4708 (IEEE, 2017).
- Weigert, M., Royer, L., Jug, F. & Myers, G. Isotropic reconstruction of 3D fluorescence microscopy images using convolutional neural networks. In *International Conference on Medical Image Computing and Computer-Assisted Intervention* (eds Descoteaux, M. et al.) 126–134 (Springer, 2017).
- Prevedel, R. et al. Simultaneous whole-animal 3D imaging of neuronal activity using light-field microscopy. *Nat. Methods* **11**, 727–730 (2014).

**Publisher's note** Springer Nature remains neutral with regard to jurisdictional claims in published maps and institutional affiliations.

© The Author(s), under exclusive licence to Springer Nature America, Inc. 2020

## Methods

**Widefield fluorescence imaging.** Widefield imaging was performed on a previously described home-built system. In these experiments, we used a  $\times 60$ , NA = 1.42 oil objective (Olympus) on an Olympus IX81 inverted microscope equipped with XT 640-W (Lumen Dynamics Group) as the illumination source and an automated  $xy$  stage with an additional  $z$  piezolectric stage (100- $\mu\text{m}$  range; Applied Scientific Instrumentation (ASI), PZ-2000). The illumination was filtered with an excitation filter (ET470/40x, Chroma) and then reflected toward the sample via a dichroic mirror (T495lpxr, Chroma). The emission was collected by the same objective and filtered with a bandpass emission filter (ET525/50m, Chroma) before imaging with an electron-multiplying charge-coupled device (EMCCD) (Evolve Delta, Photometrics). An exposure time of 20 ms and EM gain of 20 were used. The imaging axial step for both beads and fixed actin samples was 150 nm.

**Fixed phalloidin-labeled actin samples.** U2OS cells were cultured on glass-bottomed dishes (MatTek, P35G-1.5-14C) at 37°C with 5% CO<sub>2</sub>. Before labeling, cells were rinsed three times with 1× PBS, fixed with 1 ml of 4% paraformaldehyde and 2% glutaraldehyde in 1× PBS for 20 min at 37°C, rinsed twice in 2 ml of 750 mM Tris-HCl (pH 7.5) and permeabilized in 0.2% Triton X-100 in 1× PBS for 10 min. Next, samples were washed three times in staining buffer and blocked in staining buffer containing 1% BSA for 30 min. Blocking buffer was removed, and the samples were stained with 200  $\mu\text{l}$  of a 1:50 dilution of Alexa Fluor Phalloidin-488 (Thermo Fisher Scientific, A12379) diluted in 0.2% Tween-20 in 1× PBS for 1 h. Cells were washed in 0.2% Tween-20 in 1× PBS three times and imaged in 1× PBS.

**Bead samples.** Glass-bottomed dishes (MatTek, P35G-1.5-14C) were cleaned with 100% ethanol and coated with 0.1% poly(L-lysine) (Sigma-Aldrich, P8920) for 10 min. 100-nm yellow-green beads (Thermo Fisher Scientific, F8803) were diluted  $\sim 10^5$ -fold, and 20  $\mu\text{l}$  was added to the coverslip. After 10 min, the dish was washed four times with clean water before imaging. Bead images were used for estimating the widefield PSFs used in Supplementary Fig. 7.

**Confocal imaging.** Confocal imaging was performed on a Leica SP8 confocal microscope with a 1.40-NA oil lens (HCX PL APO CS 63.0X1.40 OIL UV). The power for the 488-nm argon laser was set at 20%, and the AOTF (488) was set at 5%. The sample was scanned bidirectionally with a voxel size of 48.1 nm in the  $xy$  plane and 125.9 nm in the  $z$  direction at 200 Hz with a 6× line average. The pinhole size was set to 20.1  $\mu\text{m}$  (0.21 Airy units). The fluorescence signal was collected from 510 nm to 580 nm with a Leica HyD hybrid detector operating in photon counting mode (10% gain). Data were saved in eight-bit format.

**Immunolabeled microtubule samples.** U2OS cells were cultured on No. 1.5 coverslips (Fisherbrand, 12-545-81) at 37°C with 5% CO<sub>2</sub>. Before labeling, cells were rinsed three times with 1× PBS, fixed with 1 ml methanol for 3 min at  $-20^\circ\text{C}$  and rinsed twice in 2 ml of 1× PBS. Next, samples were washed three times in staining buffer and blocked in staining buffer containing 1% BSA for 30 min. The blocking buffer was removed, and the samples were stained with 200  $\mu\text{l}$  of a 1:100 dilution of anti- $\alpha$ -tubulin primary antibody (Thermo Fisher Scientific, 322500) for 1 h. Cells were washed in 0.2% Tween-20 in 1× PBS and stained with 200  $\mu\text{l}$  of a 1:200 dilution of Alexa Fluor 488-conjugated goat anti-mouse secondary antibody (Invitrogen, A11001) diluted in 0.2% Tween-20 in 1× PBS for 1 h. Finally, cells were washed three times in 0.2% Tween-20 in 1× PBS and twice in distilled water before mounting in Prolong Diamond (Thermo Fisher Scientific, P36961).

**iSIM imaging.** The iSIM system has been previously described<sup>13</sup>. For all experiments, a  $\times 60$ , NA = 1.42 oil-immersion objective (Olympus PlanApo N 60× Oil) was used, resulting in an image pixel size of 55.5 nm and a lateral resolution of  $\sim 150$  nm. Fluorescence data were acquired with a pco.edge 4.2 sCMOS camera, and the exposure time was set to 40 ms per image frame. The imaging axial step for beads, immunolabeled mitochondrial samples and transfected endoplasmic reticulum (ER) samples was set to 100 nm, 100 nm and 500 nm, respectively.

**Immunolabeled mitochondrial samples.** U2OS cells were cultured on glass-bottomed dishes (MatTek, P35G-1.5-14C) at 37°C with 5% CO<sub>2</sub>. Before labeling, cells were rinsed three times with 1× PBS, fixed with 1 ml of 4% paraformaldehyde and 2% glutaraldehyde (Electron Microscopy Sciences, 15710 and 16120) in 1× PBS for 20 min at 37°C, rinsed twice in 2 ml of 750 mM Tris-HCl (pH 7.5) (Corning, 46-030-CM) and permeabilized in 0.2% Triton X-100 (Sigma, T9284) in 1× PBS for 10 min. Next, samples were washed three times in staining buffer (0.2% Tween-20 (Sigma, P9416) in 1× PBS) and blocked in staining buffer containing 1% BSA (Thermo Fisher Scientific, 37525) for 30 min. The blocking buffer was removed, and the samples were stained with 200  $\mu\text{l}$  of a 1:200 dilution of anti-Tomm20 primary antibody (Abcam, 78547) diluted in 0.2% Tween-20 in 1× PBS for 1 h. Cells were washed in 0.2% Tween-20 in 1× PBS and stained with 200  $\mu\text{l}$  of a 1:200 dilution of Alexa Fluor 488-conjugated donkey anti-rabbit secondary antibody (Invitrogen, A21206) for 1 h. Finally, cells were washed three times in 0.2% Tween-20 in 1× PBS and imaged in the iSIM in 1× PBS.

**Transfected ER samples.** U2OS cells were cultured in 1 ml of medium using a MatTek glass-bottomed dish at 37°C with 5% CO<sub>2</sub>. At 80% confluence, cells were transfected with 100  $\mu\text{l}$  of transfection buffer containing 2  $\mu\text{l}$  of X-treme GENE, 2  $\mu\text{l}$  of plasmid DNA (ERmoxGFP<sup>45</sup>; Addgene, 68072; 420 ng  $\mu\text{l}^{-1}$ ) and 96  $\mu\text{l}$  of PBS. Cells were imaged 1 d after transfection.

**Bead samples.** Yellow-green fluorescent beads (Thermo Fisher Scientific, F8803; 100-nm diameter) were used for experimental FWHM measurements for iSIM. Beads were diluted from the stock concentration 1:1,300 (1:100 in distilled water and 1:13 in ethanol) and spread over cleaned glass coverslips. After air-drying for 5 min, coverslips were washed twice in distilled water to remove unattached beads. After air-drying again, beads were mounted in oil (Cargille, 16241) on glass slides and sealed with nail polish.

**Zeiss Lightsheet Z.1 imaging.** Images were captured with a Zeiss Lightsheet Z.1 Selective Plane Illumination microscope (Carl Zeiss Microscopy), tandem PCO.edge sCMOS cameras (PCO.Imaging) and Zeiss Zen imaging software. A pair of Zeiss  $\times 10$ , 0.2-NA dry illumination objectives were used alongside a Zeiss  $\times 20$ , 1.0-NA long-working-distance detection objective. The illumination sheet was narrowed to 2  $\mu\text{m}$ , and images were acquired with an exposure time of 10 ms for both the green (488 nm) and red (561 nm) channels. In single-view experiments, samples were imaged dorsally with volumes acquired every 2 min. In multiview experiments, two views were collected at  $-15$  and  $+15$  degrees from dorsal, with volumes acquired every 5 min.

**Zebrafish embryos.** Imaging of the embryonic zebrafish hindbrain used three transgenic fish lines: Tg(*h2az2a:h2az2a-GFP*)<sup>46</sup>, Tg(*en.crest1-hsp70l:mRFP*)*ch100* (ref. <sup>47</sup>) and Tg(*sox10:mRFP*)*vu234* (ref. <sup>48</sup>). Adult females carrying the nuclear label *hist2h2l:GFP* were crossed to males carrying either the cranial efferent marker *en.crest1-hsp70l:mRFP* (for single-view experiments) or the neural crest marker *sox10:mRFP* (for multiview experiments). The resulting progeny were staged to 18 hours post-fertilization following standard morphological criteria<sup>49</sup>. For single-view experiments, embryos were prepared via multilayer mounting<sup>50</sup> in Fluorostore Fractional FEP Tubing (F018153-5). For multiview experiments, embryos were mounted in 1.2% agarose (Invitrogen, UltraPure Agarose, 16500) in glass capillary tubes. Specimens were immersed in embryo medium with 0.2 mg  $\text{ml}^{-1}$  tricaine and incubated at 28.5°C during data collection.

**Fiber-coupled diSPIM imaging.** We used our original fiber-coupled diSPIM system<sup>51</sup> in addition to another recently described fiber-coupled diSPIM system<sup>52</sup> to acquire volumetric time-lapse datasets of zebrafish embryo lateral line and nematode embryo neurodevelopment, respectively. Data were acquired in light-sheet scan mode (scanning the light sheet through the stationary sample) with the ASI diSPIM Micromanager<sup>53,54</sup> (<http://dispm.org/software/micro-manager>) plugin instead of the LabVIEW control software used previously<sup>51</sup>. For zebrafish data, the  $xy$  stage was manually moved periodically to ensure that the growing tip of the lateral line did not exit the field of view.

**Nematode embryos.** The 718-bp promoter in plasmid Dacr3078 (*fmi-1p*(718 bp)(EcoRV-EcoRV)::*Syn21-GFP-CAAX::p10* 3' UTR) is a bashed fragment from the 3,186-bp promoter upstream of the *fmi-1* start codon. To make plasmid Dacr3078, EcoRV was used to digest plasmid Dacr2984 (*fmi-1p*(3,186 bp)::*Syn21-GFP-CAAX::p10* 3' UTR) followed by subsequent religation. Transgenic strain DCR6371 was made by injecting plasmid Dacr3078 at 50 ng  $\mu\text{l}^{-1}$  into the lineaging strain BV514, which ubiquitously expresses *mCherry:histone* reporter constructs, *pie-1p::mCherry::H2B::pie-1* 3' UTR and *nhr-2p::his-24::mCherry::let-858* 3' UTR<sup>10</sup>. From a spontaneous integration of Dacr3078 into BV514, *olaIs98* was isolated. The integrated strain was designated DCR6371. The *Syn21-p10* 3' UTR is a translational enhancer system used in *Drosophila* to boost translational expression<sup>55</sup>. We have found that this also seems to help boost expression in *C. elegans* (unpublished results).

Worms were cultivated at 20°C on nematode growth medium seeded with a lawn of *Escherichia coli* strain OP50 using standard methods. Embryos were laid by gravid adults and picked from the plate into M9 buffer with 0.25% methylcellulose and were then pipetted onto a poly(L-lysine)-coated coverslip and imaged in M9 buffer, as previously described<sup>9</sup>. Samples were imaged every 100 s for 50 time points with both the 561-nm and 488-nm lasers. Further details are available in ref. <sup>52</sup>.

**Zebrafish embryos.** For zebrafish posterior lateral line imaging, *cldnb:lyn-GFP*<sup>26</sup> embryos at 30–32 hours post-fertilization were placed in embryo medium (60 mg RedSea Coral Pro Salt (Drs Foster and Smith Pet Supplies) per liter of ddH<sub>2</sub>O) supplemented with 600  $\mu\text{M}$  MS-222 (Sigma, E10521). For diSPIM imaging, embryos were mounted in 1% low-melt agarose (Cambrex, 50080) and covered with embryo medium; the agarose above the posterior lateral line primordium was manually removed with forceps before imaging.

**Quadruple-view light-sheet microscopy.** We modified our previously described triple-view SPIM system<sup>11</sup> to acquire four volumetric views. Two  $\times 40$ , 0.8-NA water-immersion objectives (OBJ A and OBJ B in Supplementary Fig. 9; Nikon,

MRD07420) were used in a free-space coupled diSPIM configuration<sup>9</sup>. A  $\times 60$ , 1.2-NA water-immersion objective (OBJ C in Supplementary Fig. 9; Olympus, UPLSAPO60XWPSF) was mounted beneath the coverslip. Each objective was housed within a piezoelectric objective positioner (PZT, Physik Instrumente, PIFOC-P726), enabling independent axial control of each detection objective.

Four volumetric views were obtained with the three objectives in stage scanning mode; that is, samples were translated through the light sheet via an *xy* piezo stage (Physik Instrumente, P-545.2C7; 200  $\mu\text{m} \times 200 \mu\text{m}$ ). When excitation was introduced from OBJ B, one top view (collected from OBJ A) and one bottom view (from OBJ C) were simultaneously acquired. Similarly, when illumination was introduced from OBJ A, another top view (collected from OBJ B) and bottom view (from OBJ C) were simultaneously acquired. Views collected from OBJ A and OBJ B were acquired as usual in light-sheet microscopy (that is, they were perpendicular to the illumination); views collected from OBJ C were acquired by scanning OBJ C vertically during each exposure. Thus, the top two sCMOS cameras corresponding to OBJ A and OBJ B were operated in hybrid rolling/global shutter mode, but the lower camera was operated in virtual confocal slit mode, to obtain partially confocal images during light-sheet illumination introduced from OBJ A and OBJ B.

**T cells.** E6-1 Jurkat T cells stably transfected to express EGFP–actin were grown in RPMI-1640 medium with L-glutamine and supplemented with 10% FBS, at 37 °C in a 5% CO<sub>2</sub> environment. Glass coverslips (24 mm  $\times$  50 mm  $\times$  0.17 mm; VWR, 48393241) were coated with 0.01% (wt/vol) poly(L-lysine) (Sigma-Aldrich) and incubated with anti-CD3 antibody (HIt-3a, eBiosciences) at 10  $\mu\text{g ml}^{-1}$  for 2 h at 37 °C the same day that cells were imaged. Before imaging, 1 ml of cells was centrifuged at 250 RCF for 5 min, resuspended in L-15 imaging buffer supplemented with 2% FBS and plated onto coverslips.

**Cleared-tissue imaging.** We modified our original fiber-coupled diSPIM<sup>51</sup> for cleared-tissue imaging by incorporating elements of the commercially available ASI DISPIM and DISPIM for Cleared Tissue (CT-DISPIM). All components were designed and manufactured by ASI unless otherwise specified. The microscope body was built inside an incubator box (RAMM-Incu) on a 450 mm  $\times$  600 mm breadboard (Incu-breadboard). Samples were placed on an FTP-2000 Focusing Translation Platform to provide precise and repeatable *x,y,z* positioning of the sample as well as rapid stage scanning<sup>51</sup> during cleared-tissue imaging. CAD drawings of the setup are shown in Supplementary Fig. 15.

Dovetail mounts (DV-6010) were attached to the SPIM head (SPIM-DUAL-K2) lower Cube III modules and connected to angled dovetails on support arms from posts mounted to the breadboard (Camera Support Kit CAM\_SUP-K4-13-5). This configuration fixes the SPIM head while the sample can be moved relative to the head using the FTP-2000, minimizing vignetting of the fluorescence emission, which compromised earlier diSPIM performance on large samples.

Each camera (Hamamatsu Orca Flash 4.0) was attached to a tube lens assembly (MIM-Tube-K), which was clamped to Ø1.5-inch support posts (Thorlabs) from the breadboard, leaving an air gap of 1–2 mm between the tube lens assembly and the SPIM head. The resulting vibrational decoupling of the cameras from the SPIM head minimized image jitter caused by the camera fans. The cameras themselves were additionally supported on brackets angled at 45 degrees (Thorlabs, AP45) mounted on Ø1.5-inch vibrationally damped posts (Thorlabs, DP14A).

For cleared-tissue imaging, we used a pair of Special Optics 0.4-NA cleared-tissue immersion objectives (ASI, 54-10-12). At the refractive index of the solvent we used (dibenzyl ether), the magnification of these lenses is  $\sim 17.9$ . Because the back focal planes of these objectives are at a different location than for the Nikon  $\times 40$ , 0.8-NA water-immersion objectives used for live work, the excitation scanners and their associated tube lenses were mounted to adjustable spacers (C60-SPACER-ADJ ASSEMBLY) to ensure 4*f* spacing of the light-sheet excitation path. All cleared-tissue experiments used quad notch filters (Semrock StopLine Notch Filter NF03-405/488/561/635E-25) and associated dichroic mirrors (Semrock BrightLine Laser Dichroic DiO3-R405/488/561/635-t1-25x36), which together isolated the fluorescence from the excitation light (405, 488, 561 and 637 nm from Coherent OBIS sources).

Data were acquired by moving the stage in a raster pattern with the aid of the ASI diSPIM Micromanager<sup>53</sup> plugin (<http://dispim.org/software/micro-manager>; ref. <sup>54</sup>). The number of imaging tiles/rows as well as other acquisition parameters of interest is reported in Supplementary Table 5.

Because of the volume size and speed of data acquisition during cleared-tissue imaging, it was necessary to use an NVMe solid-state drive (Samsung 960 PRO M.2 2TB) to write data during an acquisition. Data were transferred to a local 300-TB server after acquisition for longer-term storage.

**Cleared brain slab.** The mouse brain sample was prepared using the iDISCO+ procedure<sup>29</sup>. Briefly, the brain from an adult arginine vasopressin receptor 1B (*Avpr1b*-Cre  $\times$  A19 (B6.Cg-Gt(ROSA)26Sortm9(CAG-tdTOMO))Hze<sup>56</sup>; Cre-recombinase-dependent tdtTomato) mouse<sup>32</sup> (a gift from W.S. Young) was fixed by transcardiac perfusion with 4% paraformaldehyde. It was then cut into 2-mm slabs and dehydrated through a methanol series, rehydrated, immunolabeled with an antibody that recognizes tdtTomato (1:200 dilution of rabbit anti-RFP; Rockland Antibodies and Assays, 600-401-379) and an Alexa Fluor 555-conjugated secondary antibody (Invitrogen, A27039; 1:100 dilution), and then dehydrated

with a methanol series and dichloromethane before equilibration in dibenzyl ether (Sigma, 108014) and imaging.

**Cleared gut, stomach and ovary.** Mouse tissue stored in 4% paraformaldehyde was dissected and washed in 20 ml of 1× PBS for 1 h at room temperature. Desired organs were dehydrated and rehydrated in a serial dilution of methanol in water and bleached in 5% hydrogen peroxide in methanol according to the iDISCO protocol<sup>30</sup>. After rehydration, pretreated samples were stained with 400  $\mu\text{l}$  of primary antibody dilution (1:100) in PBS containing 0.5% Triton X-100 and 0.05% sodium azide and shaken at 37 °C for 4 d. Samples were washed in 5 ml washing buffer consisting of 0.5% Triton X-100 and 0.05% sodium azide in PBS on a rotator for 1 d at room temperature. The next day, samples were stained with 400  $\mu\text{l}$  of secondary antibody dilution (1:100) consisting of 0.5% Triton X-100 and 0.05% sodium azide in PBS in a 37 °C shaker for 4 d. Samples were washed for 1 d before optical clearing. For some samples, a 1:1,000 dilution of DAPI (1 mg ml<sup>-1</sup> stock) was incorporated in the first washing step. All labels are indicated in Supplementary Table 6.

Immunolabeled samples were dehydrated sequentially in 5 ml of 20%, 40%, 60%, 80%, 90% and 100% tetrahydrofuran in water (30 min at room temperature for each step). Samples were washed in 5 ml of 100% tetrahydrofuran for another 30 min at room temperature and incubated in 5 ml of 100% dichloromethane until samples sank to the bottom of the tube. Samples were then incubated overnight at room temperature in another 5 ml of fresh 100% dichloromethane. The next day, samples were cleared twice in 5 ml of dibenzyl ether (Sigma, 108014) at room temperature for 30 min each time. Cleared samples were mounted on a glass slide with a minimal amount of Krazy Glue surrounding the bottom of the samples for imaging with cleared-tissue diSPIM.

**Bead sample.** No. 1.5 coverslips (VWR, 48393241) were cleaned with 100% ethanol and coated with 0.1% poly(L-lysine) (Sigma-Aldrich) for 10 min. Then, 100-nm yellow-green beads (Thermo Fisher Scientific, F8803) were diluted  $\sim 10^5$ -fold, and 20  $\mu\text{l}$  was added to the central region of the coverslip. After 10 min, the coverslip was washed four times with clean water before imaging. During imaging, the beads were immersed in dibenzyl ether (Sigma, 108014).

**Free-space coupled diSPIM, conventional and reflective imaging.** The geometry of the diSPIM (0.8/0.8 NA) used for conventional and reflective imaging has been previously described<sup>13</sup>. Glass coverslips (24 mm  $\times$  50 mm  $\times$  0.17 mm; VWR, 48393241) for conventional experiments were modified for reflective experiments by sputtering a 150-nm-thick aluminum film over their entire surface and then protecting them with a 700-nm-thick layer of SiO<sub>2</sub> (Thin Film Coating). During conventional imaging, dual views were sequentially acquired in light-sheet scanning mode via two objectives (Nikon, MRD07420;  $\times 40$ , 0.8 NA) and imaged with 200-mm tube lenses (ASI, C60-TUBE\_B) onto two sCMOS cameras (PCO, Edge 5.5), resulting in an image pixel size of 162.5 nm. During reflective imaging, four views (direct fluorescence and mirror images) were simultaneously collected in stage scanning mode with the same detection optics. In all acquisitions, the exposure time for each plane was 5 ms.

**Nematode embryos.** *C. elegans* were maintained on nematode growth medium seeded with *E. coli* (OP50). Embryos were dissected from gravid adults, placed on poly(L-lysine)-coated coverslips and imaged in M9 buffer, as previously described<sup>9</sup>. Strain BV24 (*ltIs44(pie-1p-mCherry::PH(PLC1delta1) + unc-119(+))*; *zul178((his-72 1 kb::HIS-72::GFP); unc-119(+))*)V was used for imaging nuclei in conventional mode, and strain AQ2953 (*ltIs131(myo-3p::GCaMP3-SL2-tagRFP-T)*) was used for imaging calcium flux in threefold embryos in reflective mode.

**Lattice light-sheet microscopy, conventional and reflective imaging.** The LLS microscope (1.1, 0.71 NA) for reflective imaging was constructed as previously described<sup>14</sup>. The annular mask was set at 0.325–0.4 NA, and a square lattice in dithered mode was produced at the sample. The excitation power (488 nm) was measured at the back focal plane of the excitation objective at  $\sim 25 \mu\text{W}$ . The  $\times 25$  Nikon CFI APO LWD detection objective was paired with a 500-mm achromat lens for an effective magnification of 63.7, resulting in an image pixel size of 102 nm. The exposure time for each plane was 8 ms, and the stage scanning step size for the volumetric imaging was 0.4  $\mu\text{m}$ , corresponding to 209 nm along the optical axis after deskewing. When deconvolving the data with a spatially variant PSF for resolution recovery and removal of epifluorescence contamination<sup>13</sup>, the excitation pattern was based on the measured dimensions of the LLS (propagation distance of  $\sim 26.6 \mu\text{m}$  FWHM along the optical axis and a waist of 0.99  $\mu\text{m}$  FWHM), and the detection PSF was simulated as a widefield PSF with 1.1 NA using the PSF generator ImageJ plugin (<http://bigwww.epfl.ch/algorithms/psfgenerator/>). The light-sheet dimensions were measured by sweeping the sheet axially through a 0.1- $\mu\text{m}$ -diameter fluosphere (Thermo Fisher) while stepping the bead along the propagation length of the sheet. Conventional imaging experiments were conducted on 5-mm-diameter  $\times$  0.15 mm glass coverslips (Warner Instruments, CS-5R). For reflective experiments, 5-mm-diameter  $\times$  0.17 mm glass coverslips were sputtered as for the free-space diSPIM experiments with a 150-nm-thick film of aluminum followed by a 700-nm-thick layer of SiO<sub>2</sub> (Thin Film Coating).

**Microtubule and actin samples.** For imaging microtubules, U2OS cells (ATCC, HTB-96) were grown on uncoated coverslips, fixed with glutaraldehyde, washed with PBS at room temperature and then immunolabeled with anti-DM1A antibody conjugated with Alexa Fluor 488 (Sigma, T9026). For imaging of  $\alpha$ -actinin, U2OS cells stably transfected to express mEmerald-tagged  $\alpha$ -actinin (a gift from M. Davidson, Florida State University) were plated onto coverslips 24 h before imaging. Cells were imaged within 1 h of plating on the reflective coverslips.

**Data processing. Preprocessing.** Raw single-view and multiview images were preprocessed by subtracting a uniform background with intensity equivalent to the average of 100 dark (no excitation light) background images before registration and/or deconvolution. For deconvolution, the measured image or the average of the measured images after elimination of zero values (zeros replaced by a small value, 0.001) was used as the initial estimate. However, we note that the more rapid deconvolution reported in this work is robust to changes in the initial guess, as we obtained similar acceleration when using a constant-valued image as the initial estimate.

**diSPIM deconvolution.** The joint RLD scheme used in diSPIM improves the overall estimate  $e$  of sample density by alternately considering each view<sup>37</sup>:

$$e_0 = (i_A + i_B)/2$$

For  $k = 0, 1, \dots, N$  (i.e., iteration number)

$$\tilde{e}_k = e_k \left\{ \left( \frac{i_A}{e_k^* f_A} \right)^* b_A \right\}$$

$$e_{k+1} = \tilde{e}_k \left\{ \left( \frac{i_B}{\tilde{e}_k^* f_B} \right)^* b_B \right\}$$

where  $i_A, f_A, b_A$  and  $i_B, f_B, b_B$  are the raw images, forward projector (PSF) and back projector corresponding to views A and B, respectively. Traditionally,  $b$  is taken to be the transpose of  $f$ . However, as in single-view deconvolution, we found that using unmatched back projectors (for example, Gaussian, Butterworth or WB filters) considerably accelerated this procedure (reducing  $N$ ).

**Quadruple-view deconvolution.** In quadruple-view deconvolution, we start with the additive RLD update, finding as previously reported<sup>11</sup> that this method yields better reconstructions than the alternating joint deconvolution update<sup>37</sup> used for diSPIM:

$$e_0 = (i_A + i_B + i_C + i_D)/4$$

For  $k = 0, 1, \dots, N$  (i.e., iteration number)

$$e_A = e_k \left\{ \left[ \frac{i_A}{e_k^* f_A} \right]^* b_A \right\}$$

$$e_B = e_k \left\{ \left[ \frac{i_B}{e_k^* f_B} \right]^* b_B \right\}$$

$$e_C = e_k \left\{ \left[ \frac{i_C}{e_k^* f_C} \right]^* b_C \right\}$$

$$e_D = e_k \left\{ \left[ \frac{i_D}{e_k^* f_D} \right]^* b_D \right\}$$

$$e_{k+1} = (e_A + e_B + e_C + e_D)/4$$

with  $f, b, e$  and  $i$  defined as above and the subscripts A, B, C and D indicating each view. Choosing each back projector  $b$  to be the transpose of the forward operator  $f$  yields the traditional RL update. Choosing the back projectors as follows yields the previously described ‘virtual-view’ update in EBMD<sup>10</sup> (where  $*$  denotes convolution and  $\wedge$  denotes the transpose), speeding up this procedure:

$$b_A = \hat{f}_A (\hat{f}_A^* f_B \hat{f}_B) (\hat{f}_A^* f_C \hat{f}_C) (\hat{f}_A^* f_D \hat{f}_D)$$

$$b_B = \hat{f}_B (\hat{f}_B^* f_C \hat{f}_C) (\hat{f}_B^* f_D \hat{f}_D) (\hat{f}_B^* f_A \hat{f}_A)$$

$$b_C = \hat{f}_C (\hat{f}_C^* f_D \hat{f}_D) (\hat{f}_C^* f_A \hat{f}_A) (\hat{f}_C^* f_B \hat{f}_B)$$

$$b_D = \hat{f}_D (\hat{f}_D^* f_A \hat{f}_A) (\hat{f}_D^* f_B \hat{f}_B) (\hat{f}_D^* f_C \hat{f}_C)$$

Finally, setting  $b$  to be the unmatched WB filter appropriate for each view provides the fastest update, as for dual-view and single-view microscopes.

**Joint deconvolution for reflective light-sheet imaging.** Raw image data from the four views in reflective diSPIM imaging (0.8/0.8 NA) or two views in reflective lattice light imaging (0.7/1.1 NA) are merged to produce a single volumetric view, after processing steps that include background subtraction, interpolation, transformation, fusion, registration, epifluorescence removal and joint deconvolution. The data processing steps for removing epifluorescence contamination and enhancing resolution for reflective diSPIM and reflective LLS imaging are similar to those previously described<sup>13</sup> for the symmetric (0.8/0.8 NA) and asymmetric (0.71/1.1 NA) diSPIM configurations. We represent the effect of the mirrored coverslip by reflecting the object across the coverslip to obtain an extended object consisting of real and virtual objects. During each RL update, we construct the forward model by (1) shifting the illumination pattern at each axial ( $z$ ) slice in the extended object; (2) multiplying the shifted illumination pattern by the estimate of the extended object; (3) looping over  $z$  in the estimate and, at each  $z$ , performing 2D convolution with the detection PSF; and (4) collapsing over the  $z$  coordinate. In the backward model, we perform back projection of the ratio image (that is, the ratio of the raw data to the blurred estimate), convolve it with the appropriate back projector function (the flipped PSF for traditional RLD or the unmatched back projector for the WB case) and then multiply by the shifted illumination pattern. This deconvolution process is not blind, that is, the PSFs are simulated widefield detection PSFs based on experimentally measured PSFs. For the datasets we report here, there was no need to crop the data. When processing the reflective LLS data, the excitation profile was based on the measured dithered LLS illumination.

In more detail, we form view  $U_1$  (which includes both the conventional view and mirrored views) and a second, virtual view  $U_2$  by reflecting view  $U_1$  across the mirror, as previously described<sup>13</sup>.  $U_1$  and  $U_2$  are thus blurred with complementary detection PSFs. We register the two views  $U_1$  and  $U_2$  and perform joint deconvolution on them by applying the joint RL update with the WB back projector for each view as follows:

$$\hat{F}^{(n+1)} = \hat{F}^{(n)} \frac{1}{V_1} \left[ \mathcal{M}_{B1} \frac{U_1}{\mathcal{M}_{F1} \hat{F}^{(n)}} \right]$$

$$\hat{F}^{(n+2)} = \hat{F}^{(n+1)} \frac{1}{V_2} \left[ \mathcal{M}_{B2} \frac{U_2}{\mathcal{M}_{F2} \hat{F}^{(n+1)}} \right]$$

Here  $\mathcal{M}_{F1}$  and  $\mathcal{M}_{F2}$  are the forward operators that map the object stack to measured conventional view stack  $U_1$  and virtually reflected view stack  $U_2$  respectively, and  $\hat{F}$  and  $\mathcal{M}_{B2}$  are the backward operators that map from data space back to object space. Four steps are sequentially applied in obtaining each update. First, we compute  $\mathcal{M}_{B2}$  or  $\mathcal{M}_{F2} \hat{F}^{(n)}$  by applying the forward operator  $\mathcal{M}_{F1}$  or  $\mathcal{M}_{F2}$  to the current estimate of the object  $\hat{F}^{(n)}$  according to three cascaded operations  $\hat{F}^{(n)}$  at each light-sheet position (or  $z$  slices), where matrix  $\mathcal{D}$  represents multiplication of the estimate  $\mathcal{D}$  by the crossed light sheets; matrix  $\mathcal{H}$  represents looping over all the  $z$  slices and performing 2D convolution with a slice of the detection PSF at each  $z$ ; and matrix  $\mathcal{P}$  applies projection over all  $z$  slices. Second, we divide the measured data stack  $U$  by this quantity and denote the resulting ratio image  $R$ . Third, we apply the transpose operator  $\mathcal{P}^\top$  or  $\mathcal{M}_{B2}$  to  $R$ , which involves applying the cascaded operations  $\mathcal{D}^\top \mathcal{H}^\top \mathcal{P}^\top$  and then summing over all  $z$  slices. Here  $\mathcal{P}^\top$  is a back projection matrix, which smears the vector to which it is applied back across the image grid;  $\mathcal{H}^\top$  represents looping over  $z$  in the object distribution and performing 2D convolution with a slice of the transposed but unmatched detection PSF (that is, the WB back projector appropriate for the particular microscope; Supplementary Note 2) at each  $z$ ; and  $\mathcal{D}^\top$  is equivalent to matrix  $\mathcal{D}$ , denoting multiplication by the illumination pattern. Finally, we update the current estimate  $\mathcal{D}$  by multiplying by the correction image  $\hat{F}^{(n)}$  or  $\mathcal{M}_{B2}$  and dividing by the normalization image  $V_1$  or  $V_2$  (that is,  $\mathcal{M}_{B1} 1$  or  $\mathcal{M}_{B2} 1$ , where 1 denotes an image of ones).

**GPU deconvolution with Huygens software.** For the deconvolution comparison in Supplementary Fig. 13, both WB and Huygens deconvolution (Scientific Volume Imaging, Essential 19.10 version) use the same theoretical PSF, generated as the product of the excitation light sheet and widefield emission PSF. When testing Huygens, we used the light-sheet deconvolution module. All parameters were set at their default values. Deconvolution was performed on a Windows 10 workstation (CPU: Intel Xeon, Platinum 8168, two processors; RAM: 512 GB; GPU: Nvidia Quadro RTX6000 graphics card, 24 GB of memory).

**Conventional 3D affine registration.** Some CPU-based registrations were performed in the open-source Medical Imaging Processing, Analyzing and Visualization (MIPAV) programming environment (<http://mipav.cit.nih.gov/>). As previously described<sup>1</sup>, we applied an affine transform with 12 degrees of freedom (d.f.) to register the source image (S; image to be registered) to the target image (T; fixed image). The d.f. matrix is a 12-element transformation matrix that applies the four affine image transformation operations (translation, rotation, scaling and

shearing) from the source to the target image. We used an intensity-based method to iteratively optimize the d.f. matrix by minimizing a cost function via Powell's method (<http://mathfaculty.fullerton.edu/mathews/n2003/PowellMethodMod.html>). We set the search angle range from -10 degrees to 10 degrees, with a coarse angle increment of 3 degrees and a fine angle increment of 1 degree. This registration function 'Optimized Automatic Image Registration 3D' has already been incorporated in MIPAV as plugin 'SPIM-fusion' (ref. <sup>51</sup>). With this CPU-based registration environment, we registered the data imaged with diSPIM (Fig. 2a,j) and quadruple-view light-sheet microscopy (Fig. 2e; see below for more detail on how we registered four views) and compared the registration outcomes and computational costs with those of the GPU-based registration described in the following section (Fig. 2i). To estimate the computational costs for registering large cleared-tissue volumes with the CPU-based approach (Fig. 3i), we randomly chose ten subvolumes (each  $640 \times 640 \times 640$  pixels), calculated the time for registration, averaged the times (that is, ~31 min per subvolume) and then multiplied the averaged time by the total number of subvolumes (for example, 4,576 subvolumes in Fig. 3d) to estimate the total registration time (that is, ~100 d).

For the comparative data shown in Supplementary Table 4, registration was also performed using the NiftyReg software package (<http://cmictig.cs.ucl.ac.uk/wiki/index.php/NiftyReg>) and the elastix software package (<http://elastix.isi.uu.nl>). For NiftyReg, the reg\_aladin command was used with default settings except that the '-pv' and '-pi' parameters were both set as 100. In this case, NiftyReg performed a rigid + affine-based registration. For elastix, the transform type was set as 'AffineTransform' to perform affine-based registration; the Interpolator was set as 'LinearInterpolator', and the Resampler was set as 'DefaultResampler' for CPU implementation and 'OpenCLResampler' for GPU implementation.

**New GPU-based 3D affine registration.** We developed a new registration pipeline that accelerates the registration of multiview light-sheet data via GPU programming (Supplementary Fig. 12), including data acquired with diSPIM (Fig. 2a,j), quadruple-view light-sheet microscopy (Fig. 2e), reflective diSPIM (Fig. 4c) and reflective LLS microscopy (Fig. 4f). More notably, this GPU-based registration method also enables the registration of large cleared-tissue datasets imaged with diSPIM (Fig. 3), which is impractical if implemented in the CPU-based registration method (for example, ~100 d with CPU-based registration as estimated above versus ~24 h with GPU-based registration for the data in Fig. 3d).

Our GPU-based method uses the same method (that is, intensity-based iterative optimization of the transformation matrix) as in the CPU-based MIPAV registration but dramatically improves the registration speed and accuracy for several reasons. First, we iteratively perform affine transformations on the source image, which is always kept in the GPU texture memory. The main computational burden in 3D transformation is trilinear interpolation, which can be substantially lessened by the use of texture memory. Second, the correlation ratio between the intensity of the transformed source and target images that is used in the cost function can be rapidly calculated via the parallel computations enabled by the GPU. Third, when minimizing the cost function by using Powell's method to update the 12-element transformation matrix, we do not simultaneously optimize all 12 elements (that is, full translation, rotation, scaling and shearing, which comprise 12 d.f.). Instead, the optimization is serial, successively optimizing translation; rigid body (translation and rotation, 6 d.f.); translation, rotation and scaling (9 d.f.); and finally the full translation, rotation, scaling and shearing operations (12 d.f.). We observed that such serial optimization makes registration more accurate and robust. Finally, although the initial transformation matrix ( $M_0$ ) for beginning the optimization process is an identity matrix by default, we also provide an option to generate  $M_0$  by performing a 2D registration (translation and rotation) on the xy and zy maximum-intensity projections of the source and target images. This 2D registration is an intensity-based rigid body transformation with the same optimization routine as 3D registration, but performing registration in 2D with only translation and rotation is very rapid, only taking ~1% of the time required for performing full 3D registration. This additional step also guarantees a reasonable starting initialization of  $M_0$  for further 3D optimization in 3D. Alternatively, a transformation matrix from a previous time point in a time-lapse four-dimensional (4D) dataset can be used as  $M_0$  to accelerate registration. In some cases (for example, Fig. 2a), we observed that using a matrix from a previous time point could reduce the registration time for a new volume by as much as 65%, for example, from ~8.8 s per volume to ~3.1 s per volume.

We implemented this GPU-based registration pipeline in CUDA/C++ (Supplementary Software) and called it in MATLAB or Fiji to register the data imaged with conventional and reflective diSPIM and LLS microscopy (Figs. 2a,j and 4c,f). To increase registration accuracy for the quadruple-view data (Fig. 2e and Supplementary Fig. 10) acquired with the quadruple-view light-sheet system (Supplementary Fig. 9), we (1) transformed view A and view B into the coordinate system of bottom views C and D and deconvolved each view to increase image quality; (2) registered the deconvolved view D to the deconvolved view C, thus obtaining a registration matrix mapping view D to view C, and applied this registration matrix to the raw view D, thus registering it to the raw view C; (3) registered the deconvolved view B to the deconvolved view A, thus obtaining a registration matrix mapping view B to view A, and applied this registration matrix to the raw view B, thus registering it to the raw view A; (4) performed

joint deconvolution on the two registered raw views A and B; (5) registered the jointly deconvolved views A and B to the deconvolved view C, thus obtaining a registration matrix mapping views A and B to view C; and (6) applied both registration matrices (view B to view A and then views A and B to view C) to register all raw views to the coordinate system of the bottom views (that is, views C and D). For deconvolving time series data (Fig. 2e and Supplementary Video 6), we applied this process to the first time point in each view, obtaining a set of registration matrices that were then applied to all other time points in the 4D dataset.

**Postprocessing pipeline for large cleared-tissue data imaged with diSPIM.** We developed a postprocessing pipeline that can register and jointly deconvolve large datasets imaged with diSPIM, including the cleared-tissue data presented in this paper (Supplementary Fig. 17). Such datasets span hundreds of gigabytes to terabytes, a size that exceeded either the RAM or GPU memory on our workstation.

First, raw image data recorded by the cameras in cleared-tissue diSPIM (multiple 16-bit TIFF files, each less than or equal to 4 GB) need to be reorganized and resaved as TIFF stacks, each corresponding to a distinct spatial subvolume (tile), color and view. Second, tiles for each color and view are combined with Imaris Stitcher (based on ref. <sup>58</sup>), the ImageJ plugin implementation of BigStitcher<sup>59</sup> or custom software written in MATLAB during the revision process for this manuscript (Supplementary Fig. 18, Supplementary Table 5 and Supplementary Software).

Our custom stitching software uses two steps to compute locations for every tile with subpixel accuracy (Supplementary Fig. 18): (1) using the GPU, calculate coarse 3D translational shifts for all pairs of adjacent tiles using Fourier-based phase correlation<sup>58,59</sup> on downsampled images (final size of 512–1,024 pixels in each dimension) and (2) compute fine (subpixel) 3D translational shifts for the coarsely registered tiles using our GPU-based registration method.

In more detail, we calculate the Fourier-based phase correlation shifts according to

$$P = IFT \left\{ \frac{FT(tileA) \times \text{conj}[FT(tileB)]}{\| FT(tileA) \times \text{conj}[FT(tileB)] \|} \right\}$$

where tile A and tile B represent two adjacent overlapped tiles, 'conj' denotes conjugation, and FT and IFT represent the Fourier transform and inverse Fourier transform. The peak of the phase image stack S corresponds to the tile location in real space. However, because of the periodic nature of the Fourier shift theorem, each peak corresponds to two possible shifts in each spatial dimension, and thus there are  $2^3 = 8$  possible peaks that arise when calculating a 3D shift. We test each candidate shift by applying the shift, cropping the overlapped regions between the shifted tiles, calculating the normalized cross-correlation (NCC) between the cropped regions and selecting the candidate shift corresponding to the highest NCC. To increase the robustness of this correlation-based approach for stitching images with extensive noise or low information content, we take the logarithm of the tiles before Fourier transformation.

After coarse shifts between adjacent tiles are obtained as above, we apply the coarse shifts, crop the overlapped regions between shifted tiles and use our GPU-based registration method for computing subpixel shifts between tiles. With this two-step stitching method, we achieve the same NCC values as BigStitcher yet with a shorter processing time (for example, an NCC of 0.95 for the two tiles shown in Supplementary Fig. 18, part of the dataset shown in Fig. 3d, each tile with  $2,048 \times 2,048 \times 1,300$  pixels and a registration time of 165 s with this method versus 580 s with BigStitcher). Finally, image tiles are fused by performing linear blending between the finely aligned overlapped regions. We create weight images for each tile (Supplementary Fig. 18), multiply the tiles by the weight images and then sum the resulting weighted images together. For multicolor datasets, we apply the subpixel shifts and weighted images obtained from a single color (users have the option to choose the desired color in the software GUI) to all other colors.

Like BigStitcher, our stitching framework is able to fuse terabyte-sized volumes without needing to load the raw data into CPU RAM. Stitching the entire volume from multiple tiles is accomplished by looping across the lateral slices of tiles, stitching them and subsequently resaving as a TIFF file for each lateral slice. The overall processing time (including file I/O and stitching) of our method is competitive with those of Imaris Stitcher and BigStitcher (for example, ~15 min with our method versus ~18 min with BigStitcher and ~13 min with Imaris Stitcher for the data shown in Supplementary Fig. 18; more comparisons are listed in Supplementary Table 5). Moreover, conducting the stitching pipeline in MATLAB has the advantage that a single program can be used for the entire processing pipeline without needing to convert TIFF files to IMS format in Imaris or define an XML format as in BigStitcher. Like Imaris Stitcher, our software also provides a GUI for assisting users in loading files, organizing the order of tiles, aligning tiles, and previewing tiles before and after stitching (see the description provided in the Supplementary Software for details on using the software).

After stitching, the resulting large TIFF stacks are de-skewed (transforming from stage scanning mode to light-sheet scanning mode), interpolated (obtaining isotropic pixel resolution), rotated (transformed from the objective view to the

perspective of the coverslip), cropped (saving memory) and resaved as TIFF files (for example, ~2TB for the four colors and two views acquired for the dataset shown in Fig. 3d). Because of the large data size and our limited memory, we could not directly register the two views via our GPU card and performing the registration with CPU processing<sup>9</sup> is impractical because of the ~100-fold-slower processing that would result (Fig. 3e). Our strategy for dealing with the GPU memory bottleneck is to downsample views A and B by a factor  $\beta$ , to view A' and view B', such that the total size of the views is reduced by  $\beta^3$  (for example, 125-fold if  $\beta=5$ ). Registering these downsampled volumes can then be achieved in GPU memory, obtaining a registration matrix  $M_D$  that maps view B' to view A'. A coarse, global 3D affine transformation matrix  $M_G$  that maps view B to view A can then be derived from  $M_D$ :

$$M_D = \begin{bmatrix} s_x & m_x & n_x & t_x \\ m_y & s_y & n_y & t_y \\ m_z & n_z & s_z & t_z \\ 0 & 0 & 0 & 1 \end{bmatrix}$$

$$M_G = \begin{bmatrix} s_x & m_x & n_x & \beta t_x \\ m_y & s_y & n_y & \beta t_y \\ m_z & n_z & s_z & \beta t_z \\ 0 & 0 & 0 & 1 \end{bmatrix}$$

Here the three terms  $t_x$ ,  $t_y$  and  $t_z$  represent translations in each dimension, while the other nine terms,  $s_x$ ,  $s_y$ ,  $s_z$ ,  $m_x$ ,  $m_y$ ,  $m_z$ ,  $n_x$ ,  $n_y$  and  $n_z$ , combine scaling, rotation and shearing in 3D.

Note that  $M_G$  cannot be directly applied to view B to obtain a coarsely registered view B (again because of the large size). But  $M_G$  can be used to crop views A and B into multiple subvolumes that are sufficiently small that they can be registered (for example, ~1,000 subvolumes, each  $640 \times 640 \times 640$  pixels with an interval of  $512 \times 512 \times 512$  pixels, with 20% overlap between adjacent subvolumes in each dimension). If the position of the  $k$ th subvolume in view A is specified by the vector  $P_A^k = [x_A^k \ y_A^k \ z_A^k \ 1]$ , then the starting position of the  $k$ th subvolume in view B can be obtained by

$$P_B^k = [x_B^k \ y_B^k \ z_B^k \ 1] = P_A^k \times M_G^T = [x_A^k \ y_A^k \ z_A^k \ 1] \times M_G^T$$

After cropping, this subvolume can be coarsely registered with the corresponding cropped subvolume in view A using a new matrix  $M_S^k$ , which can be derived from the cropping position matrix ( $M_A^k$ ,  $M_B^k$ ) and global transformation matrix  $M_G$ :

$$M_A^k = \begin{bmatrix} 1 & 0 & 0 & x_A^k \\ 0 & 1 & 0 & y_A^k \\ 0 & 0 & 1 & z_A^k \\ 0 & 0 & 0 & 1 \end{bmatrix}$$

$$M_S^k = \text{inv}(M_B^k) M_G M_A^k = \begin{bmatrix} s_x & m_x & n_x & 0 \\ m_y & s_y & n_y & 0 \\ m_z & n_z & s_z & 0 \\ 0 & 0 & 0 & 1 \end{bmatrix}$$

Fine registration and joint WB deconvolution are then applied to the coarsely registered paired subvolumes of view A and view B. For each deconvolved subvolume ( $640 \times 640 \times 640$  pixels), boundary regions (45 pixels from each edge, in all three dimensions) are removed to eliminate edge artifacts, and the resulting subvolumes are resaved with a size of  $550 \times 550 \times 550$  pixels. Finally, stitching all deconvolved and newly cropped subvolumes results in the final reconstruction (for example, ~1 TB for the dataset displayed in Fig. 3d). Note that, during the stitch, linear blending is performed on the remaining overlapped regions of the adjacent subvolumes (38 pixels from each edge, in each dimension) to lessen stitching artifacts.

**Zebrafish segmentation.** For segmenting cells in the lateral line primordium (Fig. 2o,p), the ‘morphological segmentation’ feature in the MorpholibJ plugin<sup>60</sup> was used, with identical settings for raw and deconvolved images. Before segmentation, images were blurred in ImageJ using a Gaussian kernel with sigma = 1.5. A watershed tolerance of 15 and a connectivity of 26 were used during the segmentation. Cells in the raw data and successfully segmented cells in the processed images were manually counted in ImageJ.

**Full width at half maximum calculations.** All FWHM calculations were implemented in MATLAB. For statistical measures, values were averaged from ten simulated beads (Supplementary Fig. 2), ten experimental beads (Fig. 1d and Supplementary Figs. 1, 3 and 7e,f) or ten microtubule filaments (Supplementary Figs. 7d and 20e).

**Simulation of images with different SNRs.** SNR simulations were conducted in MATLAB. For the images shown in Supplementary Fig. 2, a noise-free image was

obtained by blurring ten point objects with the iSIM PSF (simulated as the product of the excitation and emission PSFs). We next added Gaussian noise (simulating the background noise of the camera in the absence of fluorescence) and Poisson noise (proportional to the square root of the signal). We defined SNR as

$$\text{SNR} = S / \sqrt{S + G^2}$$

where  $S$  is the signal defined by the average of all pixels with intensity above a threshold (here set as 1% of the maximum intensity of the blurred objects in the noise-free image) and  $G$  is the Gaussian noise (set as ten counts according to the measured s.d. of the background noise of the camera). The final images shown in Supplementary Fig. 2c were then generated by scaling the signal level  $S$  and adding noise according to the equation above to achieve the target SNR. For the images shown in Supplementary Fig. 6, the simulated ground-truth image consisted of spheres seeded at random locations and with random size and intensity, generated with ImgLib2 (ref.<sup>61</sup>; <http://imglib2.net>) and then smoothed. The ground-truth image was then blurred with the iSIM PSF and degraded with Poisson and Gaussian noise as described above. The signal level  $S$  was defined by the average intensity of all spheres. The NCC to the ground truth was also calculated as a metric to quantify the quality of the deconvolved images. The NCC is defined as

$$\text{NCC} = \frac{1}{N} \sum_{j=1}^N \frac{(e(j) - \mu_e)(o(j) - \mu_o)}{\sigma_e \sigma_o}$$

where  $N$  is the total number of image voxels and  $j$  is the index of each voxel;  $e$  is the ground-truth image;  $e$  is the deconvolved image;  $\mu_e$  and  $\mu_o$  are the average value of  $e$  and  $o$ ; and  $\sigma_e$  and  $\sigma_o$  are the s.d. of  $e$  and  $o$ .

**Bleach correction.** For several time-lapse datasets (Figs. 2a,e,j and 4c,f, and Supplementary Videos 3, 6, 17 and 18), we performed standard bleaching correction using an ImageJ plugin (Bleach Correction<sup>62</sup>; [https://imagej.net/Bleach\\_Correction](https://imagej.net/Bleach_Correction)) with the ‘simple ratio’ method.

**Defining data.** In the mitochondrial dataset acquired with iSIM (Fig. 1f, Supplementary Fig. 4 and Supplementary Video 2), we applied notch filters in Fourier space to suppress slight line artifacts in the raw data, as previously described<sup>3</sup>.

**Video compression and rendering.** The zebrafish lateral line volumes shown in Supplementary Video 9 were median filtered with a  $5 \times 5 \times 5$  kernel in Imaris 9.2.1 (Bitplane) and manually segmented with the ‘local contrast’ function at each time point to isolate the immune cell from the skin. The isolated immune cell was then further manually segmented by an absolute intensity threshold to remove unwanted pixels and finally false colored in red. The isolated lymphocyte was recreated as an independent channel and false colored in red. Supplementary Videos 10–14 were also rendered in Imaris 9.2.1 and exported as uncompressed avi files (usually multiple gigabytes in size). These files were JPEG compressed (down to several hundred megabytes) in ImageJ and then compressed again in the VLC media player using H.264 compression. In some cases, the total image size was also slightly downsampled to achieve the final file size.

**Neural network for deep learning.** We developed the DenseDeconNet neural network (Fig. 4b and Fig. 4.1 in Supplementary Note 4) by adapting a densely connected network<sup>42</sup> for 3D image data. This network consists of three dense blocks and uses multiple dense connections between convolutional layers to extract relevant features from the image volumes, learning the deblurring necessary for image reconstruction. All operations are implemented on 3D data and thus can directly incorporate 3D information contained within the image stacks to simultaneously improve axial and lateral resolution. The total number of learned parameters in our DenseDeconNet is approximately 18,000. The network is optimized using the backpropagation algorithm with the adaptive moment estimation (Adam) optimizer<sup>64</sup> and a starting learning rate that decays during the training procedure. More details about this fully convolutional network and associated validation tests are described in Supplementary Note 4.

In our DenseDeconNet, we designed our objective function with three terms: the mean square error (MSE), the structural similarity (SSIM) index and the minimum value of the output (MIN). The MSE term ensures that the difference between network outputs and ground truths is as small as possible. The SSIM term is used to preserve the global structural similarity between the network output and the ground truth. We monitor the MIN of the output to avoid negative values.

DenseDeconNet is implemented with Tensorflow framework version 1.4.0 and Python version 3.5.2 in the Ubuntu 16.04.4 LTS operating system. Training was performed on a workstation equipped with 32 GB of memory, an Intel Core i7 (8,700 K, 3.70 GHz CPU) and two Nvidia GeForce GTX 1080 Ti GPU cards with 11 GB of memory each. Kernels in the convolution layers were randomly initialized with a Gaussian distribution (mean = 0, s.d. = 0.1). For an input image stack ~80 MB in size, fully training the network with 7,000 iterations took ~57 h, but during the revision process for this manuscript we found that this training time could be substantially reduced to ~2.5 h if training was performed with a small cropped subvolume (~15 MB) instead of the entire volume.

We tested DenseDeconNet on 3D images of membranes and nuclei in live *C. elegans* embryos acquired with diSPIM, images of GCaMP3 expression in live *C. elegans* embryos acquired with reflective diSPIM and images of  $\alpha$ -actinin in live cells acquired with reflective LLS microscopy. The input data were either raw single-view image volumes or dual-view image volumes. The ground-truth data consisted of traditional RL joint deconvolution with ten iterations for diSPIM data (conventional and reflective coverslips) and RL deconvolution with the WB back projector with one iteration for reflective LLS data. All data were derived from volumetric time series ('4D' data); usually, 80% of volumes were randomly selected for training and the remaining 20% were used for validation and testing. The parameters for all datasets used in deep learning are summarized in Table 4.1 in Supplementary Note 4. More details are shown in Fig. 4 and Figs. 4.2–4.16 in Supplementary Note 4.

**Supplementary software.** We attach our software as a compressed zip file, which is also freely available and maintained through GitHub. The software includes four sets of programs for implementing (1) WB deconvolution on a variety of different microscopes; (2) rapid registration of two volumetric images, for example, for subsequent WB deconvolution; (3) registration and deconvolution of large cleared-tissue datasets, imaged with diSPIM; and (4) our convolutional neural network (DenseDeconNet) for resolution recovery. Programs run in MATLAB except for DenseDeconNet, which is written in Python. The zip file also includes a README file that explains how to run our software on a PC with specifications similar to ours (CPU: Intel Xeon, E5-2660-v4, 28 threads; RAM: 256 GB; GPU: Nvidia Quadro M6000 graphics card, 24 GB of memory).

The WB deconvolution program uses MATLAB scripts for WB single-view deconvolution of widefield fluorescence microscopy (Supplementary Fig. 7), confocal microscopy (Supplementary Fig. 7), iSIM (Fig. 1f, Supplementary Fig. 4 and Supplementary Video 3) and light-sheet fluorescence microscopy (Supplementary Fig. 7) data; WB joint deconvolution of diSPIM data acquired on glass coverslips (Supplementary Fig. 8); WB additive deconvolution of quadruple-view light-sheet imaging data acquired on glass coverslips (Fig. 2e and Supplementary Video 6); WB deconvolution for data contaminated with a spatially variant PSF taken with reflective, symmetric diSPIM (Fig. 4c and Supplementary Video 16); and WB deconvolution for data contaminated with a spatially varying PSF acquired with reflective LLS microscopy (Fig. 4f and Supplementary Video 18).

The registration program includes two main MATLAB scripts for performing affine registration with 12 d.f.: one that calls the registration function from a Dynamic-link Library (DLL) written in C++/CUDA (Supplementary Fig. 2e and Supplementary Video 6) and the other for conducting both registration and WB deconvolution for diSPIM data by calling the relevant functions from the DLL (Fig. 2a,f and Supplementary Videos 5 and 7). For program developers, we also provide the source code for the DLL in case they wish to customize their own library.

The program for registration and deconvolution of large cleared-tissue volumes imaged with diSPIM (Fig. 3 and Supplementary Videos 11–15) includes three main MATLAB scripts: the first is for stitching raw TIFF tiles with a GUI; the second is for preprocessing the stitched TIFF data by converting the data from stage scanning mode to the perspective of the coverslip; and the last script implements coarse registration, subvolume cropping, fine registration, WB joint deconvolution and stitching back into a large dataset. Associated MATLAB scripts and MEX files are also provided for reading and writing TIFF stacks, phasor registration and 3D convolution in the Fourier domain.

The last program includes two Python scripts for running DenseDeconNet with Tensorflow. These scripts are designed for single-view input training, single-view input validation (Figs. 4.2, 4.3 and 4.5 in Supplementary Note 4 and Supplementary Video 18), dual-input training and dual-input validation (Fig. 4c,f, Figs. 4.4–4.6 in Supplementary Note 4 and Supplementary Videos 16 and 17). Additionally, we provide a more user-friendly ImageJ plugin dedicated for registration and joint deconvolution (both traditional RLD and WB deconvolution) on diSPIM data. The plugin can process either single- or multicolor data. Users have the options to rotate, interpolate the two perpendicularly views for obtaining isotropic pixels before registration and generate 2D or 3D maximum-intensity projections of deconvolved images.

**Animal use ethical statement.** Mouse and zebrafish tissue used in this study were obtained under approved Institutional Animal Care and Use Committee protocols. Animal experiments complied with all relevant ethical regulations.

**Reporting Summary.** Further information on research design is available in the Nature Research Reporting Summary linked to this article.

## Data availability

The data that support the findings of this study are available from the corresponding authors upon reasonable request.

## Code availability

The code used in this study is available as Supplementary Software. A code description and several test datasets are also included. Users can also download the

code and updates from GitHub at <https://github.com/eguomin/regDeconProject>; <https://github.com/eguomin/diSPIMFusion>; <https://github.com/eguomin/microImageLib>.

## References

45. Costantini, L. M. et al. A palette of fluorescent proteins optimized for diverse cellular environments. *Nat. Commun.* **6**, 7670 (2015).
46. Pauls, S., Geldmacher-Voss, B. & Campos-Ortega, J. A. A zebrafish histone variant H2A.F/Z and a transgenic H2A.F/Z:GFP fusion protein for in vivo studies of embryonic development. *Dev. Genes Evol.* **211**, 603–610 (2001).
47. Mapp, O. M., Wanner, S. J., Rohrschneider, M. R. & Prince, V. E. Prickle1b mediates interpretation of migratory cues during zebrafish facial branchiomotor neuron migration. *Dev. Dyn.* **239**, 1596–1608 (2010).
48. Kucenas, S. et al. CNS-derived glia ensheath peripheral nerves and mediate motor root development. *Nat. Neurosci.* **11**, 143–151 (2008).
49. Kimmel, C. B., Ballard, W. W., Kimmel, S. R., Ullmann, B. & Schilling, T. F. Stages of embryonic development of the zebrafish. *Dev. Dyn.* **203**, 253–310 (1995).
50. Kaufmann, A., Mickoleit, M., Weber, M. & Huisken, J. Multilayer mounting enables long-term imaging of zebrafish development in a light sheet microscope. *Development* **139**, 3242–3247 (2012).
51. Kumar, A. et al. Dual-view plane illumination microscopy for rapid and spatially isotropic imaging. *Nat. Protoc.* **9**, 2555–2573 (2014).
52. Duncan, L. H. et al. Isotropic light-sheet microscopy and automated cell lineage analyses to catalogue *Caenorhabditis elegans* embryogenesis with subcellular resolution. *J. Vis. Exp.* <https://doi.org/10.3791/59533> (2019).
53. Edelstein, A. D. et al. Advanced methods of microscope control using mManager software. *J. Biol. Methods* **1**, e11 (2014).
54. Ardiel, E. L. et al. Visualizing calcium flux in freely moving nematode embryos. *Biophys. J.* **112**, 1975–1983 (2017).
55. Nern, A., Pfeiffer, B. D. & Rubin, G. M. Optimized tools for multicolor stochastic labeling reveal diverse stereotyped cell arrangements in the fly visual system. *Proc. Natl Acad. Sci. USA* **112**, E2967–E2976 (2015).
56. Madisen, L. et al. A robust and high-throughput Cre reporting and characterization system for the whole mouse brain. *Nat. Neurosci.* **13**, 133–140 (2010).
57. Hudson, H. M. & Larkin, R. S. Accelerated image reconstruction using ordered subsets of projection data. *IEEE Trans. Med. Imaging* **13**, 601–609 (1994).
58. Preibisch, S., Saalfeld, S. & Tomancak, P. Globally optimal stitching of tiled 3D microscopic image acquisitions. *Bioinformatics* **25**, 1463–1465 (2009).
59. Hörl, D. et al. BigStitcher: reconstructing high-resolution image datasets of cleared and expanded samples. *Nat. Methods* **16**, 870–874 (2019).
60. Legland, D., Arganda-Carreras, I. & Andrey, P. MorphoLibj: integrated library and plugins for mathematical morphology with ImageJ. *Bioinformatics* **32**, 3532–3534 (2016).
61. Pietzsch, T., Preibisch, S., Tomancak, P. & Saalfeld, S. ImgLib2—generic image processing in Java. *Bioinformatics* **28**, 3009–3011 (2012).
62. Miura, K., Rueden, C., Hiner, M., Schindelin, J. & Rietdorf, J. ImageJ plugin CorrectBleach v2.0.2. *Zenodo* <https://doi.org/10.5281/zenodo.30769> (2014).
63. Guo, M. et al. Single-shot super-resolution total internal reflection fluorescence microscopy. *Nat. Methods* **15**, 425–428 (2018).
64. Kingma, D. P. & Ba, J. Adam: a method for stochastic optimization. Preprint at <https://arxiv.org/abs/1412.6980> (2014).

## Acknowledgements

We thank O. Schwartz and the Biological Imaging Section (RTB/NIAID/NIH) for supplying the confocal microscope platform and providing technical assistance with experiments, W.S. Young (NIMH) for providing early access to the V1b mouse line, J. Daniels (ASI) for advice on integrating the multi-immersion objectives into our cleared-tissue diSPIM, M. Anthony (ASI) for providing CAD drawings of our diSPIM assembly, J. Shaw (Bitplane) for help with Imaris and the neurite tracing plugin, A. Lauziere for his feedback and discussion on the neural network portion of the work, R. Christensen for testing aspects of the registration and deep learning pipelines, E. Ardiel for helping us to acquire the embryonic GCaMP3 muscle data with reflective diSPIM, N. Stuurman for advice in developing ImageJ-compatible software, R. Heintzmann for his critical evaluation of our methods and suggestions on improving the clarity of our manuscript, and H. Eden and G. Patterson for valuable feedback on the manuscript. This research was supported by the intramural research programs of the National Institute of Biomedical Imaging and Bioengineering, the National Institute of Allergy and Infectious Diseases, the National Institute of Arthritis and Musculoskeletal and Skin Diseases, the Eunice Kennedy Shriver National Institute of Child Health and Human Development, the National Institute of Mental Health and the National Cancer Institute within the National Institutes of Health, the National Natural Science Foundation of China (61525106, 61427807, U1809204) and the National Key Technology Research and Development Program of China (2017YFE0104000, 2016YFC1300302). V.P. and A.B. acknowledge support by the National Center for Advancing Translational Sciences of the National Institutes of Health through grant number UL1-TR000430, NSF award

1528911 (to V.P.) and NSF Graduate Research Fellowship Program grant number DGE-1144082 (to A.B.). A.U. acknowledges support from NSF awards PHY-1607645 and PHY-1806903. P.L.R. acknowledges support from NIH R01EB107293. H.S., D.C.-R. and P.L.R. acknowledge the Whitman and Fellows program at MBL for providing funding and space for discussions valuable to this work. D.C.-R., R.I., A.S., W.A.M. and Z.B. were supported by NIH grant number R24-OD016474, L.H.D. was supported by a Diversity Supplement to R24-OD016474 and M.W.M. was supported by F32-NS098616. Z.B. additionally acknowledges support via NIH grant number R01-GM097576 and the MSK Cancer Center Support/Core Grant (P30-CA008748). A.S. is additionally supported by grant 2019-198110 (5022) from the Chan Zuckerberg Initiative and the Silicon Valley Community Foundation. J.C.W. also acknowledges support from the Chan Zuckerberg Initiative.

### Author contributions

Conceived the project: M.G., Y.L., H.L., Y.W., H.S. Designed experiments: M.G., Y.L., Y.S., T.L., D.D.N., M.W.M., L.H.D., I.R.-S., D.G., A.B., J.C., H.V., V.P., D.C.-R., Y.W., H.S. Performed experiments: M.G., Y.L., Y.S., T.L., D.D.N., M.W.M., L.H.D., I.R.-S., D.G., A.B., J.C., H.V., S.G., T.B.U., Y.W. Prepared samples: Y.S., T.L., D.D.N., M.W.M., L.H.D., R.I., I.R.-S., A.B., J.C., H.V., T.B.U., Y.W. Built instrumentation: T.L., H.V., Y.W. Developed and tested deep learning algorithms/software: Y.L., H.L., Y.W. Developed new registration

and deconvolution algorithms/software: M.G., Y.L., P.L.R., Y.W. Recognized link between medical imaging algorithms and improved deconvolution: P.L.R. Tested new registration and deconvolution algorithms/software: M.G., W.A.M., Y.W. Developed and tested big data pipeline: M.G., Y.S., Y.W. Contributed lineage/segmentation software and expertise: D.D.N., A.S., Z.B. Contributed samples: C.M.A., M.H., A.B.C. Wrote manuscript: M.G., Y.L., Y.S., P.L.R., Y.W., H.S. with input from all authors. All authors inspected data and contributed to the drafting of the manuscript. Supervised research: V.P., J.C.W., C.M.A., M.H., W.A.M., A.B.C., A.U., T.B.U., Z.B., D.C.-R. P.L.R., H.L., Y.W., H.S. Directed research: H.S.

### Competing interests

The authors declare no competing interests.

### Additional information

**Supplementary information** is available for this paper at <https://doi.org/10.1038/s41587-020-0560-x>.

**Correspondence and requests for materials** should be addressed to H.L. or Y.W.

**Reprints and permissions information** is available at [www.nature.com/reprints](http://www.nature.com/reprints).

## Reporting Summary

Nature Research wishes to improve the reproducibility of the work that we publish. This form provides structure for consistency and transparency in reporting. For further information on Nature Research policies, see [Authors & Referees](#) and the [Editorial Policy Checklist](#).

### Statistics

For all statistical analyses, confirm that the following items are present in the figure legend, table legend, main text, or Methods section.

n/a Confirmed

- The exact sample size ( $n$ ) for each experimental group/condition, given as a discrete number and unit of measurement
- A statement on whether measurements were taken from distinct samples or whether the same sample was measured repeatedly
- The statistical test(s) used AND whether they are one- or two-sided  
*Only common tests should be described solely by name; describe more complex techniques in the Methods section.*
- A description of all covariates tested
- A description of any assumptions or corrections, such as tests of normality and adjustment for multiple comparisons
- A full description of the statistical parameters including central tendency (e.g. means) or other basic estimates (e.g. regression coefficient) AND variation (e.g. standard deviation) or associated estimates of uncertainty (e.g. confidence intervals)
- For null hypothesis testing, the test statistic (e.g.  $F$ ,  $t$ ,  $r$ ) with confidence intervals, effect sizes, degrees of freedom and  $P$  value noted  
*Give P values as exact values whenever suitable.*
- For Bayesian analysis, information on the choice of priors and Markov chain Monte Carlo settings
- For hierarchical and complex designs, identification of the appropriate level for tests and full reporting of outcomes
- Estimates of effect sizes (e.g. Cohen's  $d$ , Pearson's  $r$ ), indicating how they were calculated

*Our web collection on [statistics for biologists](#) contains articles on many of the points above.*

### Software and code

Policy information about [availability of computer code](#)

#### Data collection

The simulated images in Fig. 1e, Sup. Figs. 2, 6 were generated using customized MATLAB 2016b scripts. Customized Python software was used to acquire iSIM images. Customized Python software was used to acquire data from free-space coupled diSPIM and reflective diSPIM imaging. Customized hybrid Python/LabVIEW software was used to acquire quad-view light-sheet images. Micromanager 2.0 (<https://micro-manager.org/>) was used to acquire wide-field images. ASI diSPIM Micromanager (<http://dispm.org/software/micro-manager>) was used to acquire images from control fiber-coupled diSPIM and Cleared-tissue diSPIM. LAS X software (Leica Microsystems, Germany) was used to acquire Leica SP8 confocal data. Zeiss Zen imaging software (Carl Zeiss, Germany) was used to collect Zeiss Lightsheet Z.1 data. All customized scripts and software are available upon request from the corresponding author.

#### Data analysis

Customized ImageJ macros, MATLAB scripts and CUDA v9.0 codes were used for data analysis. These are available upon request from the corresponding author or from GitHub at: <https://github.com/eguomin/regDeconProject>; <https://github.com/eguomin/diSPIMFusion>; <https://github.com/eguomin/microlImageLib>. Additional software was also used for comparison purpose, including Medical Imaging Processing Analyzing and Visualization (MIPAV, <http://mipav.cit.nih.gov/>), NiftyReg software package (<http://cmictig.cs.ucl.ac.uk/wiki/index.php/NiftyReg>), elastix software package (<http://elastix.isi.uu.nl>) and Huygens (Scientific Volume Imaging, Essential 19.10 version).

For manuscripts utilizing custom algorithms or software that are central to the research but not yet described in published literature, software must be made available to editors/reviewers. We strongly encourage code deposition in a community repository (e.g. GitHub). See the Nature Research [guidelines for submitting code & software](#) for further information.

## Data

Policy information about [availability of data](#)

All manuscripts must include a [data availability statement](#). This statement should provide the following information, where applicable:

- Accession codes, unique identifiers, or web links for publicly available datasets
- A list of figures that have associated raw data
- A description of any restrictions on data availability

The data that support the findings of this study are available from the corresponding author upon reasonable request.

## Field-specific reporting

Please select the one below that is the best fit for your research. If you are not sure, read the appropriate sections before making your selection.

Life sciences       Behavioural & social sciences       Ecological, evolutionary & environmental sciences

For a reference copy of the document with all sections, see [nature.com/documents/nr-reporting-summary-flat.pdf](https://nature.com/documents/nr-reporting-summary-flat.pdf)

## Life sciences study design

All studies must disclose on these points even when the disclosure is negative.

Sample size	For estimating spatial resolution, it is common that $\geq 10$ beads (or small structures) are sufficient to statistically calculate the FWHM, we used 10 in all cases (Fig. 1d, Sup. Figs. 1-3, 7, 17, 20).
Data exclusions	No data were excluded from analysis.
Replication	All imaging experiments were independently performed more than 3 times with similar results. We will add statements to indicate the number of times experiments were repeated in corresponding figure legends in the revision.
Randomization	No allocation into experimental groups was performed.
Blinding	No allocation into experimental groups was performed.

## Reporting for specific materials, systems and methods

We require information from authors about some types of materials, experimental systems and methods used in many studies. Here, indicate whether each material, system or method listed is relevant to your study. If you are not sure if a list item applies to your research, read the appropriate section before selecting a response.

### Materials & experimental systems

n/a	Involved in the study
<input type="checkbox"/>	<input checked="" type="checkbox"/> Antibodies
<input type="checkbox"/>	<input checked="" type="checkbox"/> Eukaryotic cell lines
<input checked="" type="checkbox"/>	<input type="checkbox"/> Palaeontology
<input type="checkbox"/>	<input checked="" type="checkbox"/> Animals and other organisms
<input checked="" type="checkbox"/>	<input type="checkbox"/> Human research participants
<input type="checkbox"/>	<input type="checkbox"/> Clinical data

### Methods

n/a	Involved in the study
<input checked="" type="checkbox"/>	<input type="checkbox"/> ChIP-seq
<input checked="" type="checkbox"/>	<input type="checkbox"/> Flow cytometry
<input checked="" type="checkbox"/>	<input type="checkbox"/> MRI-based neuroimaging

## Antibodies

### Antibodies used

Fig. 1f,g, Sup. Fig. 4  
 Primary antibody: Rabbit anti-Tomm20 (Abcam, Cat. # 78547, dilution 1:200);  
 Secondary antibody: donkey anti-rabbit Alexa-488 (Invitrogen, Cat. # A21206, dilution 1:200);  
  
 Fig. 2e, Sup Fig. 10: Anti-CD3 (eBiosciences, Hit-3a, dilution 1:100);  
  
 Sup. Fig. 7a  
 Primary antibody: Mouse anti-alpha Tubulin (Thermo Fisher Scientific, 322500, dilution 1:100);  
 Secondary antibody: Goat anti-mouse Alexa-488 (Invitrogen, A11001, dilution 1:200);  
  
 Sup. Fig. 20: DM1A Alexa-488 (Sigma, T9026)

For cleared tissues  
 Primary antibodies:  
 Rabbit anti RFP (Rockland, 600-401-379, dilution 1:200);  
 Mouse anti alpha-tubulin (Thermo Fisher Scientific, 322500, dilution 1:100);  
 Rabbit anti Tomm20 (Abcam, ab78547, dilution 1:100);  
 Goat anti PECAM-1 (R&D Systems, AF3628, dilution 1:100);  
 Mouse anti CD11c (Integrin αX) (Santa Cruz, sc-398708, dilution 1:100);  
 Rat anti CD11b (R&D Systems, MAB1124, dilution 1:100);  
 Secondary antibodies:  
 Goat anti Rabbit IgG (H+L) Alexa-555 (Invitrogen, A2703, dilution 1:100);  
 Donkey anti Goat IgG (H+L) AffiniPure F(ab')<sub>2</sub> Fragment Alexa-488 (Jackson ImmunoResearch, 705-546-147, dilution 1:100);  
 Goat anti Mouse IgG1 Alexa-488 (Thermo Fisher Scientific, A21121, dilution 1:100);  
 Donkey anti Rat IgG (H+L) CF-568 (Sigma, SAB-4600077, dilution 1:100);  
 Donkey anti Mouse IgG (H+L) Alexa-568 (Thermo Fisher Scientific, A10037, dilution 1:100);  
 Donkey anti Rabbit IgG (H+L) AffiniPure F(ab')<sub>2</sub> Alexa-647 (Jackson ImmunoResearch, 711-606-152, dilution 1:100);  
 Donkey anti Goat IgG(H+L) Alexa-Plus-647 (Thermo Fisher Scientific, A32849, dilution 1:100);  
 DAPI (Thermo Fisher Scientific, D1306, dilution 1:1000).  
 More details can be found in Methods and Sup. Table 4, 5.

## Validation

All the primary antibodies are commercial and have been extensively used in previous studies, and our staining pattern was compared to existing literature and images published online. The details of these antibodies and their validations can be found in manufacturer's websites (including references):  
 Rabbit anti RFP (Rockland, 600-401-379): [https://rockland-inc.com/store/Antibodies-to-GFP-and-Antibodies-to-RFP-600-401-379-O4L\\_24299.aspx](https://rockland-inc.com/store/Antibodies-to-GFP-and-Antibodies-to-RFP-600-401-379-O4L_24299.aspx)  
 Mouse anti alpha-tubulin (Thermo Fisher Scientific, 322500): <https://www.thermofisher.com/antibody/product/alpha-Tubulin-Antibody-clone-B-5-1-2-Monoclonal/32-2500>  
 Rabbit anti Tomm20 (Abcam, ab78547): <https://www.abcam.com/tomm20-antibody-mitochondrial-marker-ab78547.html>  
 Goat anti PECAM-1 (R&D Systems, AF3628): [https://www.rndsystems.com/products/mouse-rat-cd31-pecam-1-antibody\\_af3628](https://www.rndsystems.com/products/mouse-rat-cd31-pecam-1-antibody_af3628)  
 Mouse anti CD11c (Integrin αX) (Santa Cruz, sc-398708): <https://www.scbt.com/p/integrin-alpha-x-antibody-d-8>  
 Rat anti CD11b (R&D Systems, MAB1124): [https://www.rndsystems.com/products/mouse-cd11b-integrin-alpha-m-antibody-m1-70\\_mab1124](https://www.rndsystems.com/products/mouse-cd11b-integrin-alpha-m-antibody-m1-70_mab1124)

## Eukaryotic cell lines

### Policy information about [cell lines](#)

Cell line source(s)	The following cell lines were used: U2OS(ATCC), Jurkat T cell(ATCC).
Authentication	None of the cell lines used have been authenticated.
Mycoplasma contamination	Cell lines were not tested for mycoplasma contamination
Commonly misidentified lines (See <a href="#">ICLAC</a> register)	No commonly misidentified cell lines were used.

## Animals and other organisms

### Policy information about [studies involving animals; ARRIVE guidelines](#) recommended for reporting animal research

Laboratory animals	C. elegans embryos (varies from gastrulation to hatch); a 32-hour embryonic zebrafish; an adult vasopressin receptor 1B Cre X Ai9 mouse for the cleared brain slab; Fixed samples from an 8-week old female C57Black6 mouse for cleared intestine and ovary samples; Fixed E18.5 C57Black6 mouse embryo for cleared embryonic intestine and stomach samples.
Wild animals	The study did not involve wild animals.
Field-collected samples	The study did not involve samples collected from the field.
Ethics oversight	Mouse and zebrafish tissue used in this study were obtained under approved Institutional Animal Care and use Committee protocols.

Note that full information on the approval of the study protocol must also be provided in the manuscript.